INSTITUTE FOR FUSION STUDIES

DOE/ET-53088-530 IFSR #530

Nonlinear Evolution of Resistive Tearing Mode Instability with Shear Flow and Viscosity

L. OFMAN, P.J. MORRISON, and R.S. STEINOLFSON[a)]
Institute for Fusion Studies
The University of Texas at Austin
Austin, Texas 78712

December 1991

[a)] *Permanent address: Dept. of Space Sciences, Southwest Research Institute, San Antonio, TX 78288*

THE UNIVERSITY OF TEXAS

AUSTIN

Nonlinear Evolution of Resistive Tearing Mode Instability with Shear Flow and Viscosity

L. Ofman and P.J. Morrison
Department of Physics and
Institute for Fusion Studies
The University of Texas at Austin
Austin, Texas 78712
and
R.S. Steinolfson
Department of Space Sciences
Southwest Research Institute
San Antonio, TX 78228

Abstract

The nonlinear evolution of the tearing mode instability with equilibrium shear flow is investigated via numerical solutions of the resistive magnetohydrodynamic equations. The two-dimensional simulations are in slab geometry, are periodic in the x-direction, and are initiated with solutions of the linearized MHD equations. The magnetic Reynolds number S was varied from 10^2 to 10^5, a parameter V that measures the strength of the flow in units of the average Alfvén speed was varied, and the viscosity as measured by the Reynolds number S_ν satisfied $S_\nu > 10^3$. When the shear flow is small ($V < 0.3$) the tearing mode saturates within one resistive time, while for larger flows the nonlinear saturation develops on a longer time scale. The two-dimensional spatial structure of both the flux function and the stream function distort in the direction of the equilibrium flow. The magnetic energy release decreased

and the saturation time increased with V, for both small and large resistivity. The validity of the numerical solutions was tested by verifying that the total energy and the magnetic helicity were conserved. Total energy dissipation rate dE/dt decreases as the tearing mode approached its saturated state.

I. Introduction

The resistive tearing instability is an important phenomena in laboratory and space plasma and was first studied in its linear regime by Furth *et al.*, 1963. The instability grows in a narrow layer of the plasma where the resistivity term dominates the local magnetic field term in Ohm's law and thereby allows the field lines to tear or reconnect, and form magnetic islands. The linear growth rate of the tearing mode scales as $S^{-3/5}$ where S is the magnetic Reynolds number (defined below).

Large shear flow motions have been observed between the footpoints of solar flares as well as along field lines (Wang and Zirin, 1990), where tearing and reconnection may occur (Priest, 1985). The analytic linear theory of the tearing mode with equilibrium shear flow and viscosity has been considered by several authors (Paris and Sy, 1983; Dobrowolny *et al.*, 1983; Porcelli, 1987; Chen and Morrison, 1990a, 1990b). These studies conclude that flows approaching the Alfvén velocity can greatly modify the stability criteria of the tearing instability. This was also shown to hold numerically in the linear regime for a single tearing mode (Einaudi and Rubini, 1986, 1989; Ofman *et al.*, 1991).

Nonlinear saturation of the tearing mode occurs within one or several growth times and the growth slows down from exponential to algebraic (Rutherford, 1973). Numerical evolution of the nonlinear tearing mode (without flow) in slab geometry was studied by Schnack, 1977, and Schnack and Killeen, 1979 using the finite difference alternative direction implicit (ADI) approach. The energetics, growth rate and spatial behavior for several values of resistivity and for both constant-ψ and non-constant-ψ regimes were investigated by Steinolfson and Van Hoven, 1984. The effect of plasma rotation on the nonlinear tearing mode was considered recently by Persson and Bondeson, 1990, and Persson 1991. They solved the reduced MHD equations with the spectral approach, and found that when flow is sufficiently strong,

the viscosity sufficiently small, and the $m = 2/n = 1$, $m = 4/n = 2$ modes are present, the nonlinear evolution of the tearing mode can lead to nonlinear oscillatory behavior. These nonlinear oscillations were obtained analytically by Chen and Morrison, 1991 using center manifold reduction.

Here, the nonlinear evolution of the tearing mode with equilibrium shear flow parallel to the magnetic field is investigated numerically via solution of the incompressible two-dimensional resistive MHD equations in slab geometry using the finite difference ADI method. We find that the presence of equilibrium shear flow can reduce the amount of magnetic energy release, increase the saturation time, and can affect the topology of the field and currents generated by the instability.

The paper is organized as follows: In Sec. II the nonlinear MHD equations in slab geometry, the initial magnetic field configuration, the equilibrium flow profiles and the relevant conservation relations are presented. In Sec. III we present the numerical method of solution. Section IV is devoted to the numerical results, and a summary is given in Sec. V.

II. MHD Equations

We assume that collisional MHD theory (see e.g. Drake, 1977) is applicable, that the plasma is incompressible with constant isotropic resistivity η and constant perpendicular viscosity (Braginskii, 1965) ν, and that gravitational effects are negligible. The basic equations in cgs units are:

$$\rho\left[\frac{\partial \mathbf{v}}{\partial t} + (\mathbf{v}\cdot\nabla)\mathbf{v}\right] = -\nabla P + \frac{1}{4\pi}(\nabla\times\mathbf{B})\times\mathbf{B} + \nu\nabla_\perp^2\mathbf{v} \tag{1}$$

$$\frac{\partial \mathbf{B}}{\partial t} = \nabla\times(\mathbf{v}\times\mathbf{B}) - \frac{c^2\eta}{4\pi}\nabla\times(\nabla\times\mathbf{B}) \tag{2}$$

$$\nabla\cdot\mathbf{v} = 0\,, \qquad \nabla\cdot\mathbf{B} = 0\,, \tag{3}$$

where c is the speed of light, ρ is the constant plasma density, $\mathbf{B}$ is the magnetic field, $\mathbf{v}$ is the plasma velocity, and P is the plasma pressure. We use Cartesian geometry (with unit vectors $\mathbf{e_x}, \mathbf{e_y}$ and $\mathbf{e_z}$ and choose equilibrium magnetic and velocity fields of the form:

$$\mathbf{B} = B_0(y)\mathbf{e_x} + \nabla_\perp \psi \times \mathbf{e_z} \equiv \nabla_\perp \Psi \times \mathbf{e_z} \tag{4}$$

$$\mathbf{V} = V_0(y)\mathbf{e_x} + \nabla_\perp \phi \times \mathbf{e_z} \equiv \nabla_\perp \Phi \times \mathbf{e_z} \tag{5}$$

where Ψ and Φ are the total flux and stream functions, and ψ, ϕ are the flux and stream functions relative to the equilibrium quantities B_0 and V_0.

Substituting Eqs. (4) and (5) in Eqs. (1)–(3), taking the curl of Eq. (1), thus eliminating the pressure P, and considering the $\mathbf{e}_x - \mathbf{e_y}$ components in dimensionless form gives the following 2-D MHD equations

$$\frac{\partial \psi}{\partial t} = -\left(\frac{\partial \phi}{\partial y} + G\right)\frac{\partial \psi}{\partial x} + \left(\frac{\partial \psi}{\partial y} + F\right)\frac{\partial \phi}{\partial x} + \frac{1}{S}\nabla_\perp^2 \psi$$

$$\frac{\partial(\nabla_\perp^2 \phi)}{\partial t} = -\left(\frac{\partial \phi}{\partial y} + G\right)\frac{\partial(\nabla_\perp^2 \phi)}{\partial x} + \frac{\partial \phi}{\partial x}\left[\frac{d^2 G}{dy^2} + \frac{\partial(\nabla_\perp^2 \phi)}{\partial y}\right] + \left(\frac{\partial \psi}{\partial y} + F\right)\frac{\partial(\nabla_\perp^2 \psi)}{\partial x} \tag{6}$$

$$-\frac{\partial \psi}{\partial x}\left[\frac{d^2 F}{dy^2} + \frac{\partial(\nabla_\perp^2 \psi)}{\partial y}\right] - \frac{1}{S_\nu}\nabla_\perp^4 \phi\,, \tag{7}$$

where $\nabla_\perp^2 \equiv \frac{\partial^2}{\partial x^2} + \frac{\partial^2}{\partial y^2}$ and $\frac{\partial}{\partial z} = 0$. We have also assumed that the equilibrium magnetic field is maintained by an external electric field and we imagine a similar agent maintains the equilibrium flow. The coordinates are referenced to the magnetic shear length scale a_b, the time to the Alfvén time τ_h (given below), magnetic field to $B = |\mathbf{B}_0(y \to \infty)|$.

The dimensionless parameters are the magnetic Reynolds number $S = \tau_r/\tau_h$, the viscous Reynolds number $S_\nu = \tau_v/\tau_h$, and the shear parameter $R = a_b/a_v$, where a_v is the velocity shear length scale. The relevant time scales in these definitions are the resistive time τ_r , the Alfvén time τ_h and the viscous time τ_v given by

$$\tau_h = \frac{a_b(4\pi\rho)^{1/2}}{B}\,, \qquad \tau_r = \frac{4\pi a_b^2}{c^2\eta}\,, \qquad \tau_\nu = \frac{\rho a_b^2}{\nu}\,.$$

The quantities F and G are the normalized equilibrium magnetic and velocity field, respectively, in the x-direction. We assume that F is given by

$$F(y) = \tanh(y) \tag{8}$$

and present results for each of the following velocity profiles

$$G(y) = V \tanh(Ry) \; ; \tag{9a}$$

or

$$G(y) = V\{1 - \mathrm{sech}(Ry)\} \tag{9b}$$

where V is the velocity parameter in units of the Alfvén velocity V_a. Hereafter we refer to Eq. (9a) as the tanh velocity profile and to Eq. (9b) as the sech velocity profile. The geometry of the tearing mode in Cartesian coordinates, and the equilibrium quantities are shown in Fig. 1. In Fig. 1a , the tanh velocity profile is shown, thus V_0 and B_0 have the same dependence on y. The two flow profiles and their derivatives (i.e., flow shear) are shown in Fig. 1b. It is evident that the tanh flow profile has the largest shear at $y = 0$ (the tearing layer), and the sech flow has the largest shear away from the tearing layer.

Resistive reconnection of the B_y component of the magnetic field across the tearing layer is measured by the change in the magnetic flux across $y = 0$

$$\Delta\hat{\Phi}(t) \equiv \int_0^{x_{\max}} \left| \frac{\partial}{\partial x'} \psi(x', 0, t) \right| dx' \; , \tag{10}$$

where $x_{\max}$ is one period for the periodic boundary conditions. The nonlinear growth rate $p(t)$ is given by

$$p(t) = \frac{\partial}{\partial t} \Delta\hat{\Phi}(t) \; . \tag{11}$$

The growth rate calculated from Eq. (11) agrees with that for linear tearing (when the instability is in the linear regime) for both $V = 0$ (Steinolfson and Van Hoven 1984) and

$V \neq 0$ (Ofman *et al.*, 1991). Additional relevant quantities are the changes of the magnetic and kinetic energies relative to the equilibrium values ; i.e.

$$\Delta E_M(t) = \int_{y_{\min}}^{y_{\max}} \int_0^{x_{\max}} \left[\left(F + \frac{\partial \psi}{\partial y} \right)^2 + \left(\frac{\partial \psi}{\partial x} \right)^2 - F^2 \right] dx\, dy \ , \tag{12a}$$

$$\Delta E_K(t) = \int_{y_{\min}}^{y_{\max}} \int_0^{x_{\max}} \left[\left(G + \frac{\partial \psi}{\partial y} \right)^2 + \left(\frac{\partial \phi}{\partial x} \right)^2 - G^2 \right] dx\, dy \ , \tag{12b}$$

The total magnetic and kinetic energy

$$E_{\rm tot}(t) = \Delta E_M(t) + \Delta E_K(t) + E_{M0} + E_{K0} \ , \tag{12c}$$

where E_{M0} and E_{K0} are the initial magnetic and kinetic energies stored in the equilibrium shear flow and magnetic field. Because of resistive and viscous dissipation $E_{\rm tot}$ satisfies

$$\frac{dE_{\rm tot}}{dt} = 2 \int_{y_{\min}}^{y_{\max}} \int_0^{x_{\max}} \left[-\frac{J}{S} (J - F') - \frac{1}{S_\nu} \omega (\omega - G') \right] \ , \tag{13a}$$

where $J = -\nabla^2 \psi$ is the nonequilibrium current in z-direction, and $\omega = -\nabla^2 \phi$ is the nonequilibrium vorticity. The resistive dissipation of the magnetic helicity is given by

$$\frac{d}{dt} \int_{y_{\min}}^{y_{\max}} \int_0^{x_{\max}} \psi \, dx\, dy = -\frac{1}{S} \int_{y_{\min}}^{y_{\max}} \int_0^{x_{\max}} J \, dx\, dy \tag{13b}$$

is also of interest. Equations (13) are valid for the periodic x and zero y boundary conditions and are used as a means of estimating the quality of the numerical solutions by comparing the calculated values of the r.h.s and the l.h.s of the equations. Equation (13a) is also used to estimate the effective viscous dissipation that arises in the numerical solution of the MHD equations.

III. Method of Solution

We initiate the nonlinear computations with the solutions of the linearized version of Eqs. (6) and (7) (see, Ofman *et al.*, 1991). The amplitude factors of the linearized growing solutions

are chosen so that the nonlinear terms as calculated from the linear ϕ and ψ, are important. This procedure insures that the nonlinear code is initiated at an amplitude where the subsequent evolution of the mode is in the nonlinear regime (Steinolfson and Van Hoven, 1984). In this study the normalized spatial wavenumber $\alpha = 2\pi/\lambda$ was 0.5, which implies that the size of the longest wavelength λ in the x-direction is 4π in units of a_b. An alternating direction implicit (ADI) finite-difference technique was used to obtain the nonlinear evolution. The solutions are first advanced one half time step in the x-direction using the initial linear solutions. Next, the solutions are advanced another half time step in the y-direction using the finite difference results in the x-direction from the previous half time step. This procedure for a single time step is repeated until the full temporal evolution is obtained. In the x-direction the finite difference form of Eqs. (6) and (7) is given by the following:

$$\frac{2}{\Delta t}\psi_{i,j}^{n+1/2}+G_j\delta_x\psi_{i,j}^{n+1/2}-F_j\delta_x\phi_{i,j}^{n+1/2}+\delta_x\psi_{i,j}^{n+1/2}\delta_y\phi_{i,j}^{n}-\delta_y\psi_{i,j}^{n}-\delta_y\psi_{i,j}^{n}\delta_x\phi_{i,j}^{n+1/2}=\frac{2}{\Delta t}\psi_{i,j}^{n}-\frac{1}{S}J_{i,j} \tag{14a}$$

$$\frac{2}{\Delta t}\omega_{i,j}^{n+1/2}+\left(\delta_y\phi_{i,j}^{n}+G_j\right)\delta_x\omega_{i,j}^{n+1/2}-\left(G_j''-\delta_y\omega_{i,j}^{n}\right)\delta_x\phi_{i,j}^{n+1/2}+\left(\delta_y\psi_{i,j}^{n}+F_j\right)\delta_xJ_{i,j}^{n+1/2}$$
$$+\left(F_j''-\delta_yJ_{i,j}^{n}\right)\delta_x\psi_{i,j}^{n+1/2}=\frac{2}{\Delta t}\omega_{i,j}^{n}+\frac{1}{S_\nu}\left(\delta_x^2+\delta_y^2\right)\omega_{i,j}^{n} \tag{14b}$$

where

$$J_{i,j}^{n}=-\left(\delta_x^2+\delta_y^2\right)\psi_{i,j}^{n},\quad \omega_{i,j}^{n}=-\left(\delta_x^2+\delta_y^2\right)\phi_{i,j}^{n}\ .$$

The grid spacing in the x-direction is uniform, thus the finite differences are given by

$$\delta_x\psi_{i,j}^{n}=\frac{\psi_{i+1,j}^{n}-\psi_{i-1,j}^{n}}{2\Delta x}\ ,\quad \delta_x^2\psi_{i,j}^{n}=\frac{\psi_{i+1,j}^{n}-2\psi_{i,j}^{n}+\psi_{i-1,j}^{n}}{(\Delta x)^2}\ ,$$

while in the y-direction

$$\delta_y\psi_{i,j}^{n}=\frac{1}{2}\left(\frac{\psi_{i,j+1}^{n}-\psi_{i,j}^{n}}{y_{j+1}-y_j}+\frac{\psi_{i,j}^{n}-\psi_{i,j-1}^{n}}{y_j-y_{j-1}}\right),\quad \delta_y^2\psi_{i,j}^{n}=\frac{1}{y_{j+1}-y_{j-1}}\left(\frac{\psi_{i,j+1}^{n}-\psi_{i,j}^{n}}{y_{j+1}-y_j}-\frac{\psi_{i,j}^{n}-\psi_{i,j-1}^{n}}{y_j-y_{j-1}}\right).$$

The variable grid spacing $\Delta y_j = y_{j+1} - y_j$ expands from a minimum of $\Delta y_{\min} = 10^{-3}$ at the tearing layer to $\Delta y_{\max} = 0.5$ near the computational boundaries according to the prescription

$$\Delta y_j=\Delta y_{\max}\left(\frac{\Delta y_{\min}}{\Delta y_{\max}}\right)^{(j_{\max}-j)/(j_{\max}-1)}$$

where $j_{\max}$ denotes the boundary grid point. Up to 200 grid points in the y-direction, and up to 64 grid points in the x-direction were used. Constant grid spacing in y-direction was also used for low S values. Fourth order smoothing (Strauss, 1978) was applied to the solutions away from the tearing layer. Equations (14) are written in tridiagonal form

$$-A_i^n\, U_{i+1,j}^{n+1/2} + B_i^n\, U_{i,j}^{n+1/2} - C_i^n\, U_{i-1,j}^{n+1/2} = D_{i,j}^n \tag{15}$$

where A, B, C are 2 by 2 matrices, and U, and D are two-dimensional vectors. Equation (15) is solved for U using Gaussian elimination. For the next half time step $n \rightarrow n+1/2$ and $n+1/2 \rightarrow n+1$ in the above Eqs. (15), and the solutions are advanced one time step. The boundary conditions are $\psi(y = \pm y_{\max}) = 0$, $\phi(y = \pm y_{\max}) = 0$ where $y_{\max}$ is the distance to the boundary from the tearing layer, and both ψ and ϕ are periodic in the x-direction. Due to the presence of the symmetry breaking equilibrium shear flow one cannot use the simplifying symmetry assumptions that enable the solutions of the MHD equations to be computed in one quarter of the present domain (Steinolfson and Van Hoven, 1984). Also, the imposing of the periodic boundary conditions requires one to pass through the mesh three times for each integration in the x-direction (Schnack, 1977). Only two passes through the mesh are necessary in the non periodic y-direction.

For a fully implicit scheme the time step Δt is limited to the size of Δx; i.e., $\Delta t < \Delta x$ (Pritchett *et al.*, 1980). In our case the terms higher than second order are treated explicitly, and it has been found that the relation $\Delta t < \Delta x/2$ gives satisfactory results. When non constant grid spacing is used, Δx is one or several orders of magnitude larger than Δy across the tearing layer. Reasonable computation times on Cray II for S as large as 10^6 are possible with this technique. A typical run with $S = 10^4$ takes about 30 minutes of CPU time.

IV. Numerical Results

In Figs. 2–12 we examine the spatial structure and the temporal evolution of the nonlinear tearing mode with flow. In these runs the parameters were $S = 10^2, 10^4, 10^5, R = 0.73, \alpha = 0.5$, and the flow parameter was $V = 0, 0.1, 0.2, 0.3, 0.5$ for the tanh profile, while $V = 0.1, 0.5$ for the sech flow profile.

The spatial variations of ψ, ϕ, Ψ, Φ, and the current $J_T = J - F'$ after two resistive times, normalized to their respective maximal values are shown in Figs. 2–6. In Fig. 2 the equilibrium shear flow is the tanh velocity profile, with $V = 0.1$ and $V = 0.2$. In Fig. 3 the equilibrium shear flow is the sech velocity profile with $V = 0.1$ and $V = 0.5$. The other parameters are $S = 10^2$, $R = 0.73$, and $\alpha = 0.5$. When $V = 0$, ψ is symmetric with respect to the x and y axes, while ϕ is anti-symmetric in both the linear and nonlinear regimes. When flow is present this symmetry is broken and the perturbations align themselves with the equilibrium flow, namely, in Fig. 2, ψ and ϕ deform in opposite directions with respect to the x axis and the distortion away from the tearing layer increases with V. Similar alignment with the flow occurs for sech equilibrium in Fig. 3, but for larger V the values of ψ and ϕ are distorted more near the tearing layer (where the shear is zero) than away from it, in agreement with the stabilizing effect of higher shear regions (see, Fig. 1b) as expected from the linear theory (see, Chen and Morrison, 1990).

The contour lines of the total flux and stream functions for the tanh flow profile at $t = 200\tau_h$, with $V = 0.5$ and $S = 100$ are shown in Fig. 4. The velocity and the magnetic field lines are parallel to the contours of Ψ and Φ. The magnetic field lines exhibit the saturated island structure, where the island width is an order of magnitude larger than the tearing layer width ϵ. Similar island structures appear in the contour plot of Φ. The appearance of the stream function is different from the standard FKR case due to the presence of the equilibrium shear flow. Note that the x-point in the center of contour plot of Φ is distorted

in agreement with the structure of ϕ in Fig. 2b and small distortion of the magnetic x-point appears in the contour plot of Ψ. We present the low resistivity solutions with $S = 10^4$, $V = 0.1$, and the sech flow profile at $t = 2000\tau_h$ in Fig. 5. In Fig. 5a contours of Ψ and Φ are shown, while in Fig. 5b displays the contours of ψ and ϕ. The saturated magnetic island structure is evident in the contours of Ψ . The width of the islands is an order of magnitude larger than the width of the tearing layer. For $S = 10^4$ both the tearing layer width and the island width are smaller than for $S = 10^2$ as expected from the linear ϵ scaling with resistivity. The appearance of sharp features along the y axis indicates the narrow tearing layer. It is interesting to compare the contours of ψ in Fig. 5b to the contours of ψ in Fig. 3a. In both figures similar sharp features form along the y axis, indicating that the tearing layer is narrow compared to the high resistivity, low shear flow cases. In Fig. 5b this is due to the low resistivity ($S = 10^4$ with $V = 0.1$), while in Fig. 3a this is due to the high shear flow ($V = 0.5$ with $S = 10^2$). For the sech profile the flow near the y axis is small compared to the flow away from the y axis, and thus the contour of Φ shows a relatively flat region of width a_b along the y axis, where ϕ and its vortices are dominant. The effect of the narrow boundary layer is clearly seen in Fig. 5b.

The current J_T for $V = 0$ and $V = 0.3$ (tanh velocity profile) is shown in Fig. 6. When $V = 0$ the current is symmetric with respect to the x and y axes and its maximum $J_{T\mathbf{max}}$ occurs near the center of the slab and points in the negative z-direction. When $V = 0.3$ the current has a more complicated two-dimensional structure, again aligned with the equilibrium flow. Additional regions of significant current appear far from the tearing layer, around $y = \pm 2.5$ with $|J_T(x, 2.5)/J_{T\mathbf{max}}| \sim 0.2$, thus the flow generates significant currents in the external regions of the tearing mode.

We initiate the nonlinear evolution with a single linear mode in the x-direction. Its wavelength, and hence the size of the computational domain in the x-direction, is determined by the value of α. In Fig. 7 the solutions ψ and ϕ for the tanh profile with $V = 0.3$ are plotted

as functions of x for $y = 0.5$. A single mode corresponding to $\alpha = 0.5(x_{\max} = 2\pi/\alpha = 4\pi)$ is present, and the phase shift between ψ and ϕ is caused by the equilibrium flow. Detailed treatments of the linear tearing mode with flow are given in Einaudi and Rubini, 1990, and Ofman *et al.*, 1991.

Figure 8 depicts the temporal evolution of the growth rate, the reconnected flux and the perturbed magnetic, kinetic, and total energies for 8 resistive times ($800\tau_h$) with $V = 0.1$, the tanh flow profile, and $S = 10^2$. In Fig. 8a we present the temporal evolution of the growth rate (curve A) and the reconnected flux (curve B). Initially the growth rate calculated from Eq. (11) corresponds to the linear growth calculated directly from the exponential growth of the solutions (Ofman *et al.*, 1991), and the reconnected flux grows exponentially with time. After $10\tau_h$ the growth rate drops considerably and the reconnected flux grows linearly with time as expected in Rutherford regime (Rutherford, 1973). After another $100\tau_h$ the growth of the reconnected flux slows to less than the linear rate and after $400\tau_h$ the mode saturates completely and the amount of the reconnected flux remains practically constant with time. The growth rate continues to decrease at an exponential rate.

In Fig. 8b curve A represents the change of the magnetic energy in the x component of the magnetic field ΔE_{Mx}, (defined by setting $\partial\psi/\partial x = 0$ in Eq. (12a)) while curve B represents the change of the magnetic energy in the y component, ΔE_{My} (defined by $\Delta E_M = \Delta E_{Mx} + \Delta E_{My}$). Curve C corresponds to the total change of the magnetic and kinetic energies $\Delta E_{\rm tot} \equiv \Delta E_m + \Delta E_k$. All these quantities are presented on a log scale, thus their absolute values are shown — ΔE_{Mx} and $\Delta E_{\rm tot}$ are negative for most of the evolution time indicating energy loss. The changes of sign of $\Delta E_{\rm tot}$ and ΔE_{Mx} appear as sharp minima at $t \approx 5$ and $t \approx 30$, respectively. Most of the transfer of energy occurs from the x component of the magnetic field to the y component (curve B) and to resistive dissipation. A small fraction of ΔE_{My} is transferred to the kinetic energies (see Table I). The change of the kinetic energies ΔE_K in Fig. 8c is initially comparable in magnitude (but opposite

in sign) to ΔE_M, but after about one resistive time ΔE_{Kx} saturates at values an order of magnitude smaller than ΔE_M, and the transition from exponential to linear growth occurs in a time $t < 100\tau_h$, when ΔE_{Ky} is an order of magnitude smaller than ΔE_{Kx}.

In Fig. 9 we compare the change in the magnetic and total energies for the cases $V = 0.2$ and $V = 0.3$ with $S = 10^2$. For $V = 0.3$ the rate of change of the energies is initially ($t < 100\tau_h$) lower than for $V = 0.2$, but after the growth saturates the changes occur at similar rates. The initial wiggling of the total energy is due to transient effects that arise when the nonlinear code is initiated with the linear solutions. The total energy release of the tearing mode with $V = 0.3$ is only 60% of the energy released when $V = 0.2$. This decrease of energy release with increasing V is a trend seen in all runs as evidenced in Table I.

The case where $S = 10^4$, $V = 0.5$, with the tanh equilibrium flow profile is presented in Fig. 9 up to a time $2000\tau_h$. The temporal behavior of the $S = 10^4$ case is similar to the $S = 10^2$ case, but as expected from the lower resistivity, proceeds on a longer time scale. The absolute values of the magnetic and total energy changes are shown in Fig. 10a. Note, that the change of sign of $E_{\rm tot}$ (curve C) occurs at $\sim 700\tau_h$ that is about an order of magnitude smaller than for $S = 10^2$. This is consistent with the linear growth rate scaling of $S^{-1/2}$ for the tearing mode with flow. In Fig. 10b total energy dissipation (curve A) is compared to the resistive dissipation (curve B). Due to an initial transient instability the total energy dissipation exhibits rapid oscillations that decay within several hundred Alfvén times, and the evolution proceeds with the resistive dissipation being significantly larger than the dissipation due to numerical viscosity. The quantities ΔE_{Kx} and ΔE_{Ky} are shown in Fig. 10c. The initial exponential growth slows down after only $500\tau_h$ and the nonlinear saturation is evident. The change in the kinetic energies after $1000\tau_h$ is an order of magnitude lower than the change in the magnetic energies in Fig. 10a, thus the energy release is dominated by resistive effects. Nonlinear saturation of the growth rate (curve A) and the reconnected flux (curve B) are presented in Fig. 10d. The growth rate defined in

Eq. (11) decreases by a factor of 2 after $2000\tau_h$ and the slower than exponential growth of the reconnected flux is evident after $500\tau_h$. This is consistent with the nonlinear saturation of the energies in Figs. 10a and 10b.

In Fig. 11 we present the temporal evolution of the energies for $S = 10^5$, $V = 0.5$ and the tanh flow profile. The initial ΔE_{Mx} is 1.5 times larger than ΔE_{Mx} in the case where $S = 10^4$, and it becomes negative after $\sim 1400\tau_h$. Its slower evolution is consistent with the $S^{-1/2}$ linear growth rate scaling, and due to the large resistive time the nonlinear effects are still not significant after $2000\tau_h$ or $0.02\tau_r$. The kinetic energies in Fig. 11b evolve with the corresponding linear growth rate. From the previous results for $S = 10^2$ and $S = 10^4$ it is evident that the nonlinear saturation becomes significant on a time scale of $0.1\tau_r$ that corresponds to $10^4\tau_h$ for $S = 10^5$.

Figures 12a and 12b are devoted to the calculation of the conservation relations of Eqs. (13). As a test of the overall behavior of the numerical code we calculated the temporal change in the total energy, and the magnetic helicity for $V = 0.3$ with the tanh profile, and compared it to the resistive dissipation according to Eq. (13a) and (13b). After an initial transit period of $\sim 20\tau_h$ a very good agreement is seen between the calculated energy dissipation and the resistive dissipation. The initial ($\lesssim 30\tau_h$) energy discrepancy is due to transient numerical solutions excited initially in the nonlinear code. Values of the actual viscosity S_ν in the code were estimated using the energy conservation relation (Eqs. (13)) and were found to be $10^3 - 10^5$. The obtained values of S_ν were found to depend strongly on the amount of the numerical fourth order smoothing applied to the solutions. In the case of helicity the conservation was two order of magnitude better than the resistive energy dissipation.

The final distribution of energies for several values of V with the tanh and sech equilibrium flow, and with $S = 10^2$, 10^4 is summarized in Table I. The calculated distribution of energies for the cases with $V = 0$ agrees with the results obtained by Steinolfson and Van Hoven,

1984. When $S = 10^2$ (as noted above) the change in the magnetic energy decreases with V, while the change in the kinetic energy increases with V. When $V = 0.3$ the release of the the magnetic energy is approximately 3 times lower, and the change in total energy $\Delta E_{\rm tot}$ is 6 times lower than for $V = 0$. At the same time ΔE_{Kx} increased by 50% and ΔE_{Ky} increased by a factor of ~ 3. When $S = 10^4$ and $V = 0.5$ the release of the magnetic energy is 47% of ΔE_{Mx} when $V = 0.1$, and less than a quater of energy released without equilibrium flow. When $V = 0.5$ the change in the kinetic energies is an order of magnitude smaller than the change in the magnetic energy, and when $V = 0.1$, ΔE_K is two orders of magnitude smaller than ΔE_M. The kinetic energy is even less significant when $V = 0$.

V. Summary

We have investigated the effect of equilibrium shear flow on the evolution of the nonlinear tearing mode via numerical solution of incompressible resistive MHD equations, with V ranging up to $0.5V_a$, and S up to 10^5. The perturbed flow and stream functions loose the symmetries of the $V = 0$ tearing mode and are found to distort in the direction of the equilibrium shear flow. Their mode structure in the x-direction, determined initially by the linear wavenumber α is not greatly affected during the the nonlinear evolution. Additional currents are generated far from the tearing layer by the presence of relatively small shear flow, in agreement with the linear result that flow has a significant affect on the external region of the tearing mode. The amount of the released magnetic energy decreased with V, for both low resistivity ($S = 10^4$) and high resistivity ($S = 10^2$) tearing. Exponential decrease of the growth rate, and the corresponding saturation of the reconnected flux occurred in all the calculated cases; its time scale was primarily determined by the resistivity and the shear flow. Nonlinear saturation of the energies was found to occur after 0.1 τ_r. The change in the kinetic energy was seen to be two orders of magnitude lower than the magnetic energy release for small V, and one order of magnitude lower for large $V = 0.5$. The total energy

and helicity dissipation were calculated and found to agree with that predicted by theory.

One potential application of the present results is to flaring loops, a phenomenon that occurs when magnetic flux tubes rise through the sheared magnetic fields of solar active regions. The loops often have flows parallel to their axis (Priest, 1981) and, hence, most likely parallel to the magnetic field. It is well known that the growth of the usual tearing mode without flow and with classical dissipation is an order of magnitude too slow to explain the rapid energy release in such loops (Sturrock, 1980). The growth rate can be increased, of course, if the dissipative effects are somehow increased by nonclassical effects, such as turbulence. However, no generally accepted theory has been developed for such enhanced dissipation. Therefore, at least for classical dissipation, the present results predict that the tearing mode is even *less* likely to play a role in the energy release in flaring loops with flows.

Acknowledgments

This work was supported by the U.S. Department of Energy Contract No. DE-FG05-80ET-53088 and National Science Foundation Contract No. ATM-90-15705.

References

1. S. I. Braginskii, Rev. Plasma Phys. **1**, 205 (1965).

2. X.L.Chen, and P. J. Morrison, Phys. Fluids B **2**, 495 (1990).

3. X.L.Chen, and P. J. Morrison, Phys. Fluids B **2**, 2575 (1990).

4. X.L. Chen, and P.J. Morrison, Phys. Fluids B, to appear in April, 1992.

5. M. Dobrowolny, P. Veltri, and A. Mangeney, J. Plasma Phys. **29**, 303 (1983).

6. J.F. Drake and Y.C. Lee, Phys. Fluids **20**, 134 (1977).

7. G. Einaudi, and F. Rubini, Phys. Fluids **29**, 2563 (1986).

8. G. Einaudi, and F. Rubini, Phys. Fluids B **1**, 2224 (1989).

9. H.P. Furth, J. Killeen, and M.N. Rosenbluth, Phys. Fluids **6**, 459 (1963).

10. L. Ofman, X.L. Chen, P.J. Morrison, and R.S. Steinolfson, Phys. Fluids B **3**, 1364 (1991).

11. R. B. Paris and W. N.-C. Sy, Phys. Fluids **26**, 2966 (1983).

12. M. Persson, Ph.D. thesis, Chalmers University of Technology, Göteborg, 1987.

13. M. Persson and A. Bondeson, Phys. Fluids B **2**, 2315 (1990).

14. M. Persson, Nucl. Fusion **31**, 382 (1991).

15. F. Porcelli, Phys. Fluids **30**, 1734 (1987).

16. E.R. Priest, *Solar Magnetohydrodynamics* (Reidel, Dordrecht, The Netherlands,1985).

17. E.R. Priest, *Solar Flare Magnetohydrodynamics* (Gordon and Breach, New York) Ch. 5, 1981.

18. P.L. Pritchett, Y.C. Lee, J.F. Drake, Phys. Fluids **23**, 1368 (1980).

19. P.H. Rutherford, Phys. Fluids **16**, 1903 (1973).

20. D.D. Schnack, Ph.D. thesis, University of California, Davis, 1977.

21. D.D. Schnack and J. Killeen, Nucl. Fusion **19**, 877 (1979).

22. R.S. Steinolfson and G. Van Hoven, Phys. Fluids **27**, 1207 (1984).

23. H.R. Strauss, J. Comp. Phys. **28**, 437 (1978).

24. P. Sturrock, *Solar Flares* (Colorado Associated University Press, Boulder, CO) pp. 83-117, 1980.

25. H. Wang and H. Zirin, BAAS **22**, 2 (1990).

Figure Captions

1. The initial equilibrium magnetic field and flow.

   (a) The tanh dependence on y for $\mathbf{B}_{x0}$ and$\mathbf{V}_{x0}$.

   (b) Equilibrium flow profiles $G(y)$ and their derivatives used in the present work.

2. Spatial dependence of the flux and stream functions with $S = 10^2$, and tanh equilibrium flow profile

   (a) The flux function ψ with$V = 0.1$ (top figure) and $V = 0.2$ (bottom figure).

   (b) The stream function ϕ with $V = 0.1$ (top figure), and $V = 0.2$ (bottom figure).

3. Spatial dependence of the flux and stream functions with $S = 10^2$, and sech equilibrium flow profile

   (a) The flux function ψ with $V = 0.1$ (top figure) and $V = 0.5$ (bottom figure).

   (b) The stream function ϕ with $V = 0.1$ (top figure) and $V = 0.5$ (bottom figure).

4. The total flux function Ψ and the total stream function Φ with $V = 0.5$, $S = 10^2$, and the tanh flow profile.

5. Countour plot of the flux and stream functions with $V = 0.1$, $S = 10^4$, and the sech flow profile.

   (a) Ψ and Φ

   (b) ψ and ϕ

6. Contour plot of the current $J = -\nabla^2\psi$ with $V = 0.0$ (top figure), and $V = 0.3$ (bottom figure) and the tanh flow profile for $S = 10^2$.

7. The mode structure of ψ and ϕ with $V = 0.3$ and the tanh equilibrium flow profile for $S = 10^2$.

8. The temporal evolution for the case where $S = 10^2$, $V = 0.1$ with the tanh equilibrium flow profile.

   (a) The growth rate p (curve A) and the reconnected flux $\Delta\hat{\Phi}$ (curve B).

   (b) The change in the x component (curve A), and in the y component (curve B) of the magnetic energy. The change in the total energy (curve C).

   (c) The change in the x component (curve A), and in the y component (curve B) of the kinetic energy.

9. As in Fig. 9a but with $V = 0.2$ (top figure), and $V = 0.3$ (bottom figure).

10. The nonlinear evolution of the $S = 10^4$, $V = 0.5$ tearing mode with the tanh equilibrium flow profile.

    (a) The change in the x component (curve A), and in the y component (curve B) of the magnetic energy. The change in the total energy (curve C).

    (b) The total energy dissipation $dE_{\rm tot}/dt$ (curve A), and the resistive dissipation (curve B).

    (c) The change in the x component (curve A), and in the y component (curve B) of the kinetic energy.

    (d) The temporal evolution of the growth rate (curve A) and the reconnected flux (curve B).

11. The nonlinear evolution for the case where $S = 10^5$, $V = 0.5$ with the tanh equilibrium flow profile.

(a) The change in the x component (curve A), and in the y component (curve B) of the magnetic energy. The change in the total energy (curve C).

(b) The change in the x component (curve A), and in the y component (curve B) of the kinetic energy.

12. Numerical test of the energy and helicity conservation relations with $S = 10^2$.

(a) The energy dissipation as calculated from the l.h.s. of Eq. (13a) (curve A), and the r.h.s. of Eq. (13a) (curve B).

(b) The magnetic helicity dissipation as calculated from l.h.s. of Eq. (13b) (curve A), and the r.h.s. of Eq. (13b) (curve B).

Table I: The change in the magnetic, kinetic, and total energies.

V	ΔE_{Mx}	ΔE_{My}	ΔE_{Kx}	ΔE_{Ky}	ΔE_{tot}
$S = 10^2$, $t = 200\tau_h$					
0.0	-0.792	0.488	$0.94 \cdot 10^{-2}$	$0.73 \cdot 10^{-3}$	-0.294
tanh flow profile					
0.1	-0.482	0.305	$1.24 \cdot 10^{-2}$	$2.71 \cdot 10^{-3}$	-0.162
0.2	-0.296	0.189	$1.76 \cdot 10^{-2}$	$5.71 \cdot 10^{-3}$	$-8.37 \cdot 10^{-2}$
0.3	-0.237	0.153	$2.58 \cdot 10^{-2}$	$9.86 \cdot 10^{-3}$	$-4.83 \cdot 10^{-2}$
$S = 10^4$, $t = 2000\tau_h$					
0.0	$-9.11 \cdot 10^{-2}$	$4.38 \cdot 10^{-2}$	$1.44 \cdot 10^{-5}$	$4.74 \cdot 10^{-7}$	$-4.73 \cdot 10^{-2}$
tanh flow profile					
0.1	$-4.46 \cdot 10^{-2}$	$2.12 \cdot 10^{-2}$	$0.22 \cdot 10^{-3}$	$0.16 \cdot 10^{-3}$	$-2.30 \cdot 10^{-2}$
0.5	$-2.08 \cdot 10^{-2}$	$0.88 \cdot 10^{-2}$	$2.02 \cdot 10^{-3}$	$1.51 \cdot 10^{-3}$	$-8.47 \cdot 10^{-3}$
sech flow profile					
0.1	$-3.25 \cdot 10^{-2}$	$1.53 \cdot 10^{-2}$	$5.50 \cdot 10^{-5}$	$2.45 \cdot 10^{-5}$	$-1.72 \cdot 10^{-2}$
0.5	$-1.15 \cdot 10^{-2}$	$5.43 \cdot 10^{-3}$	$4.07 \cdot 10^{-4}$	$9.64 \cdot 10^{-5}$	$-5.59 \cdot 10^{-3}$

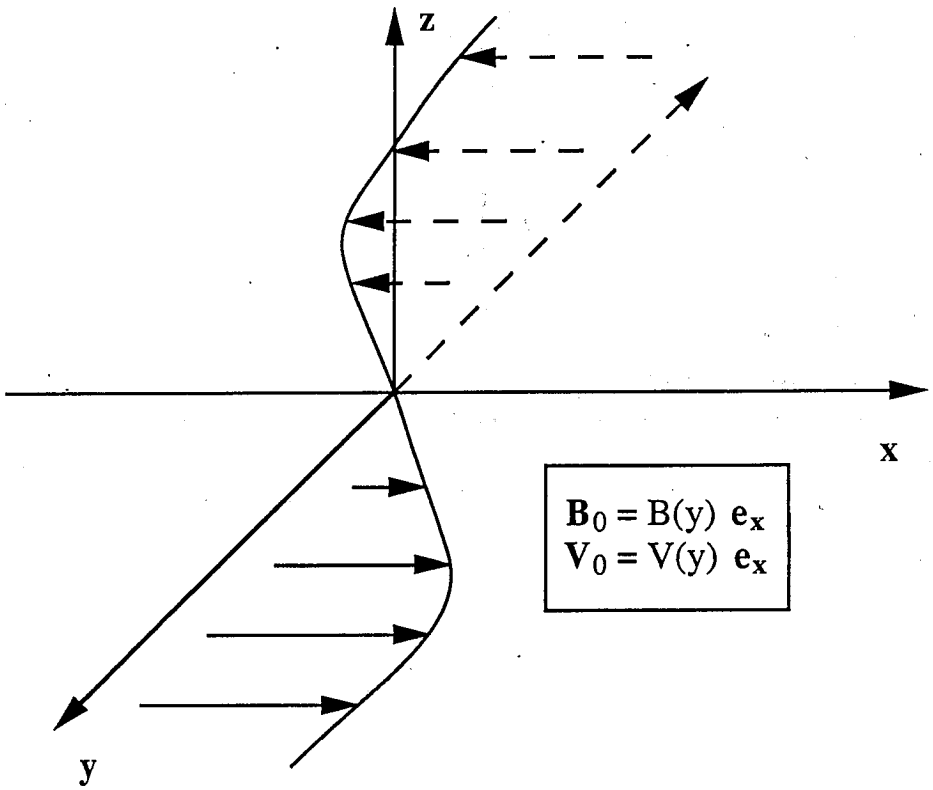

Fig. 1(a)

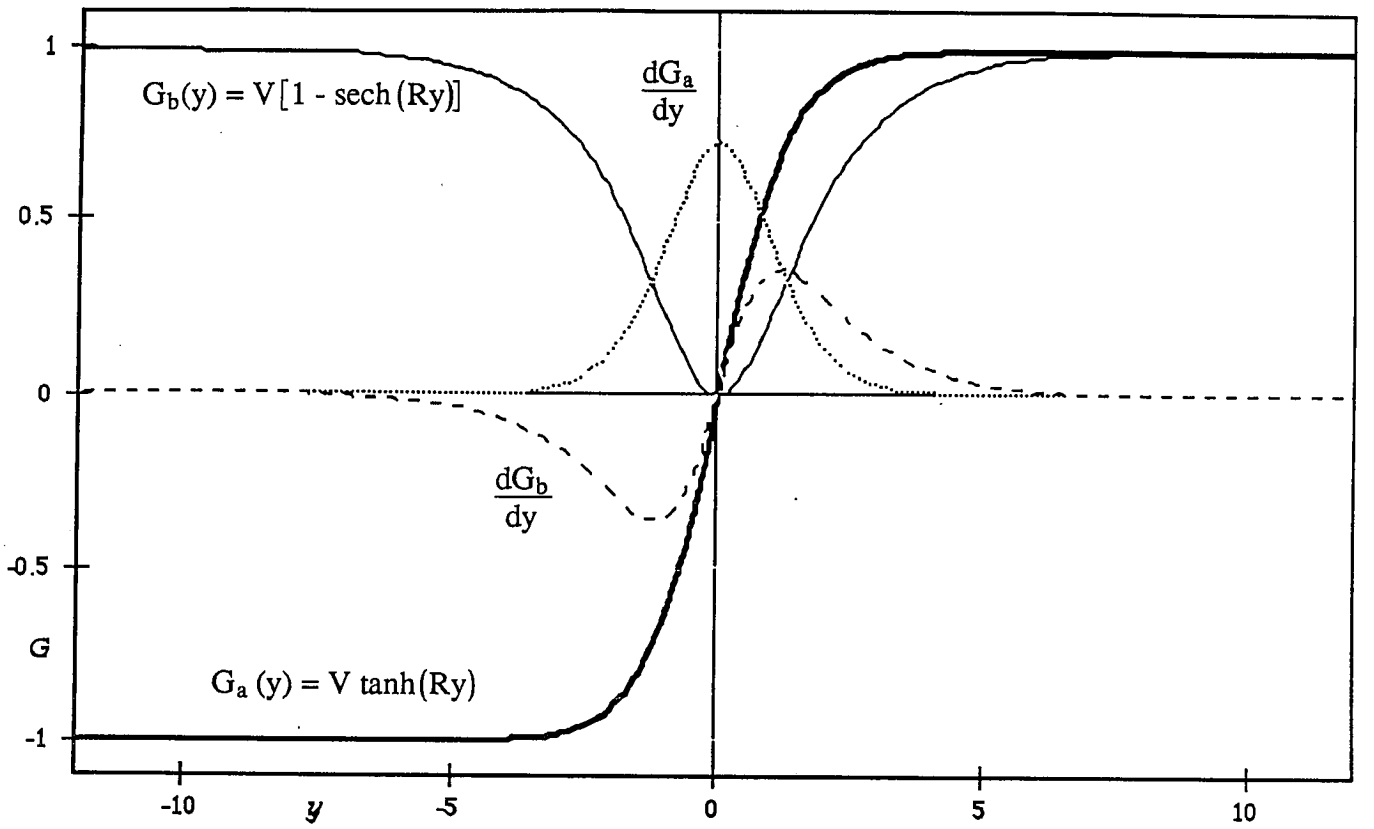
1
0.5
0
-0.5
-1
G
$G_b(y) = V[1 - \mathrm{sech}(Ry)]$
$\frac{dG_a}{dy}$
$\frac{dG_b}{dy}$
$G_a(y) = V \tanh(Ry)$
-10
-5
0
5
10
y

Fig. 1(b)

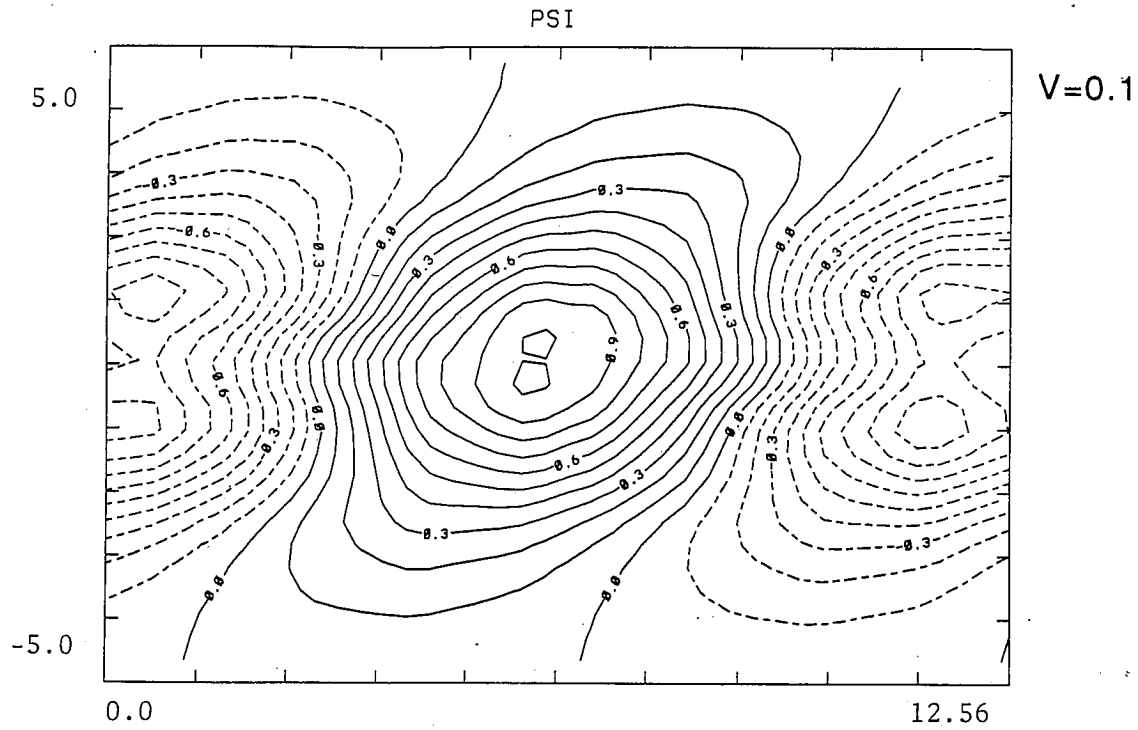

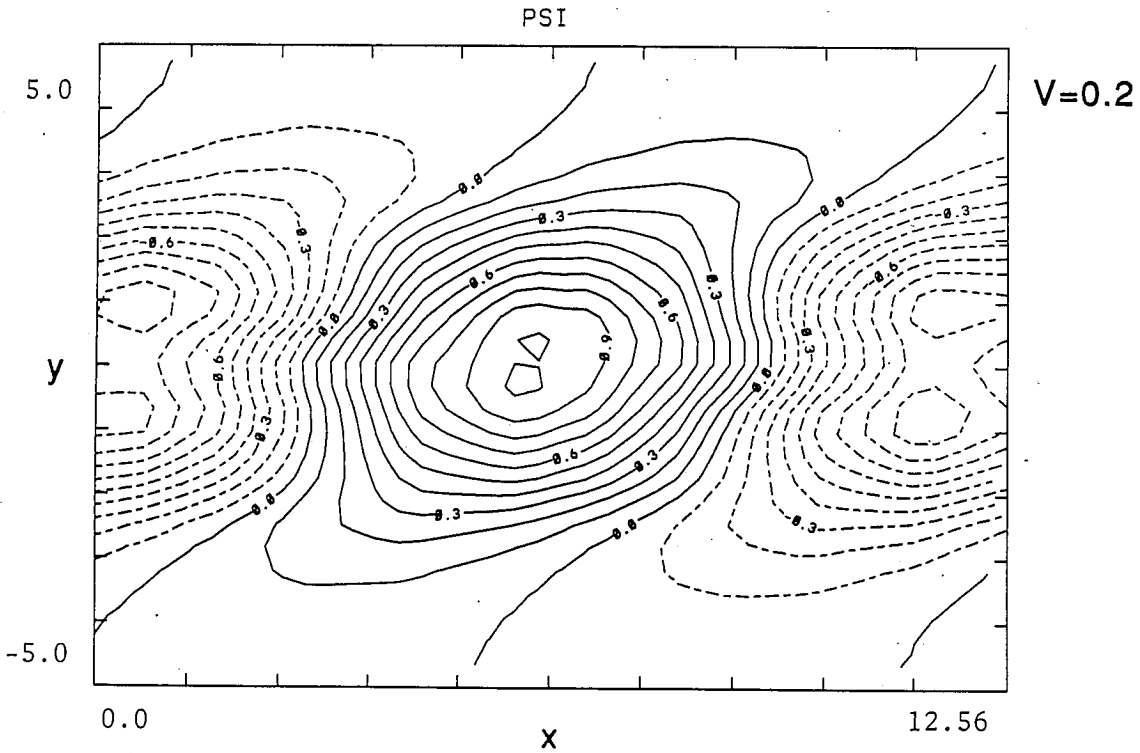

Fig. 2(a)

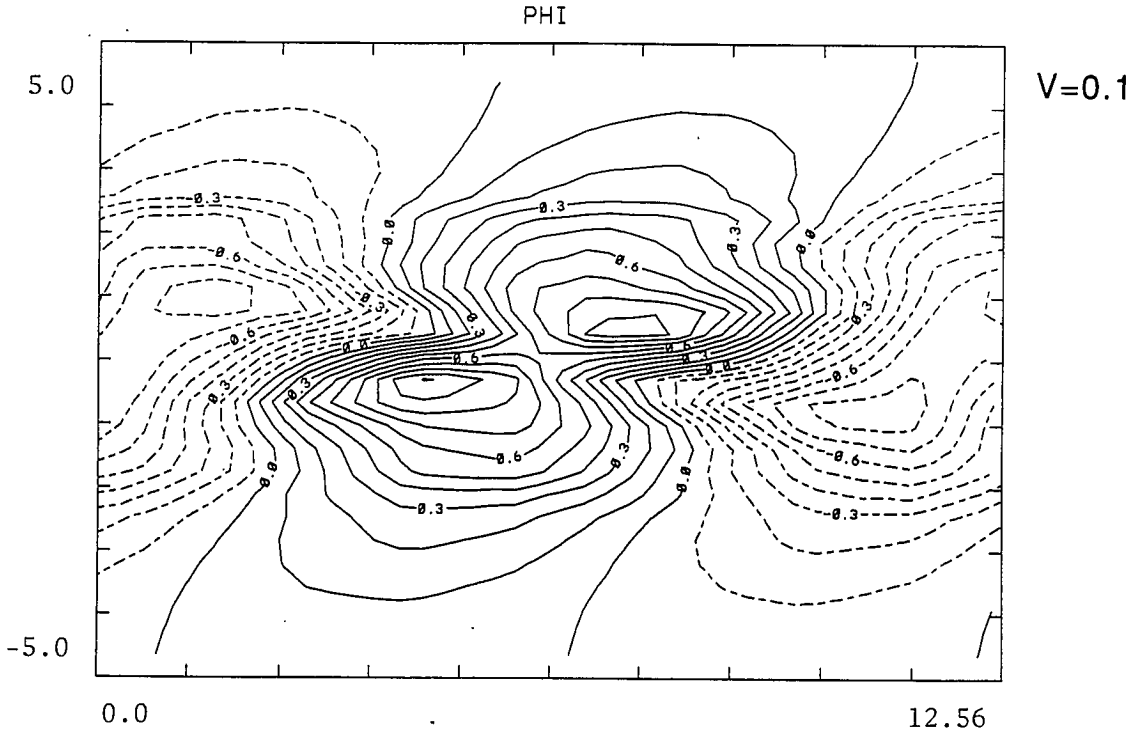

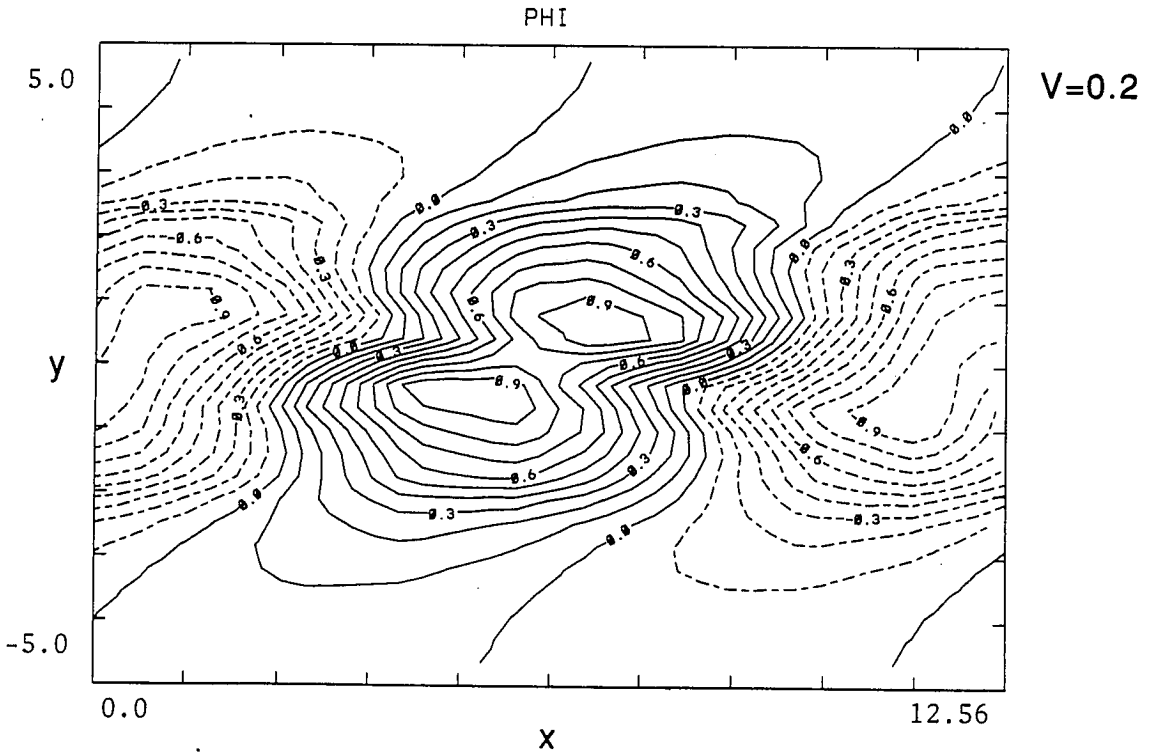

Fig. 2(b)

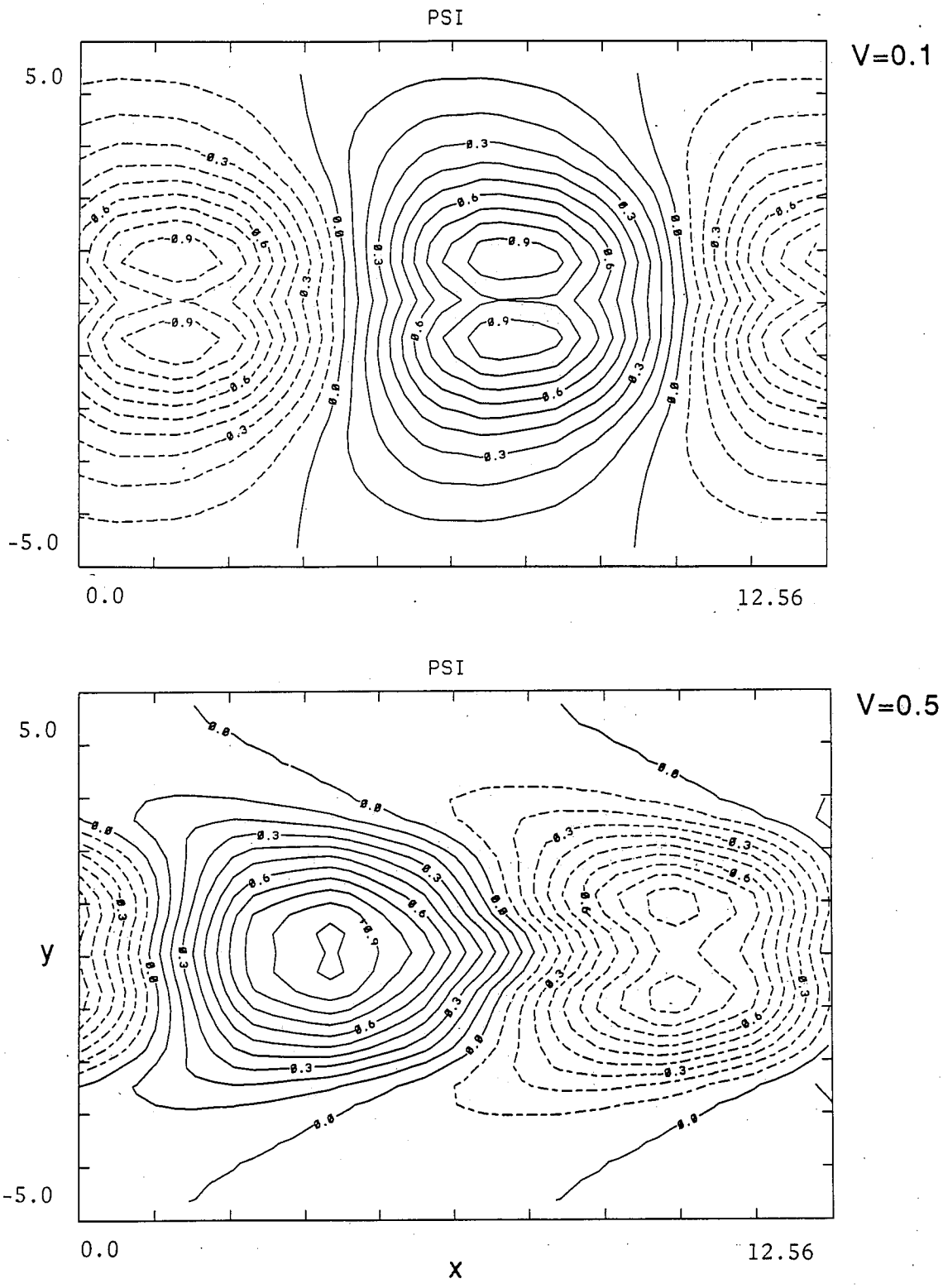

Fig. 3(a)

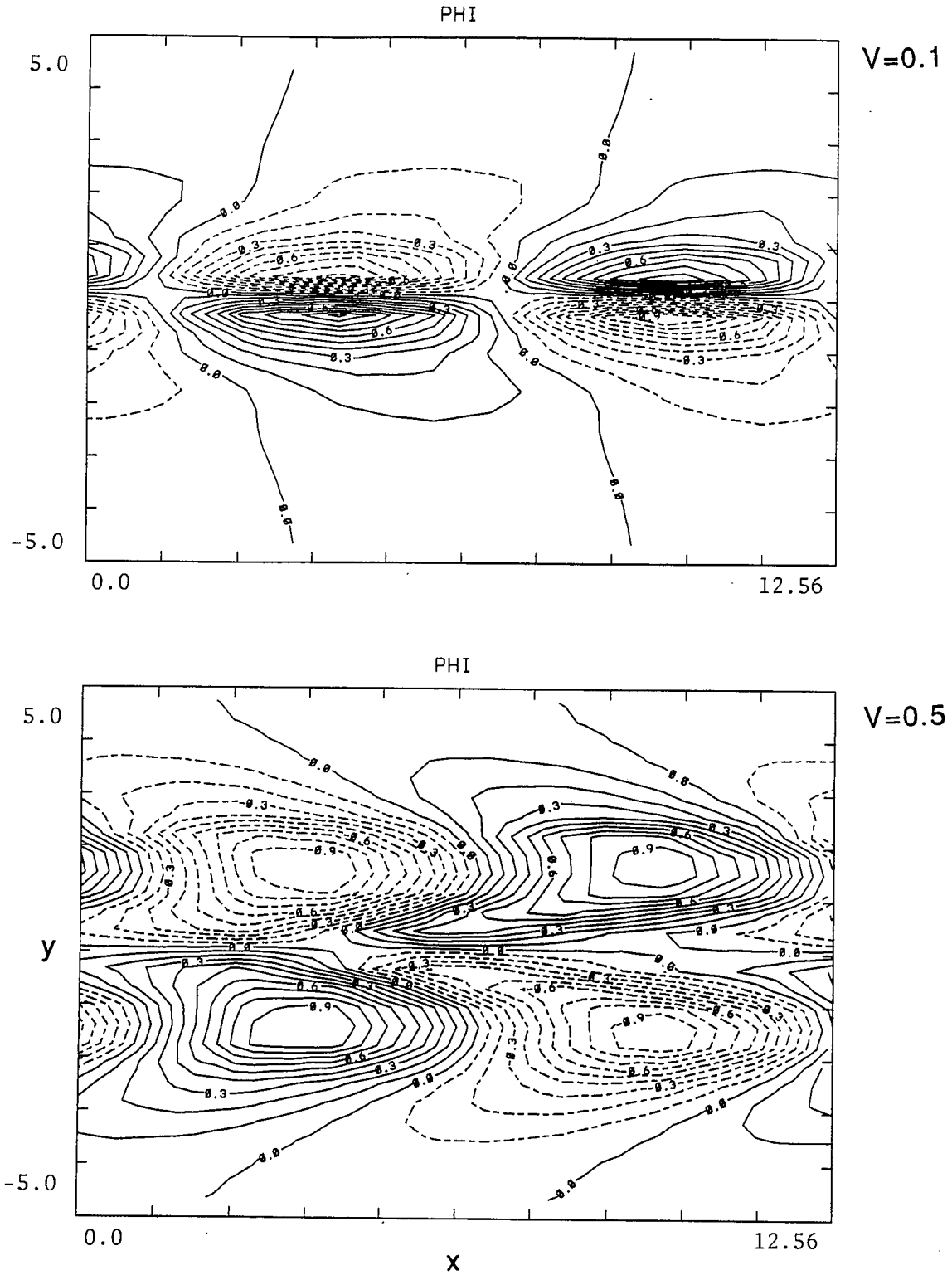

Fig. 3(b)

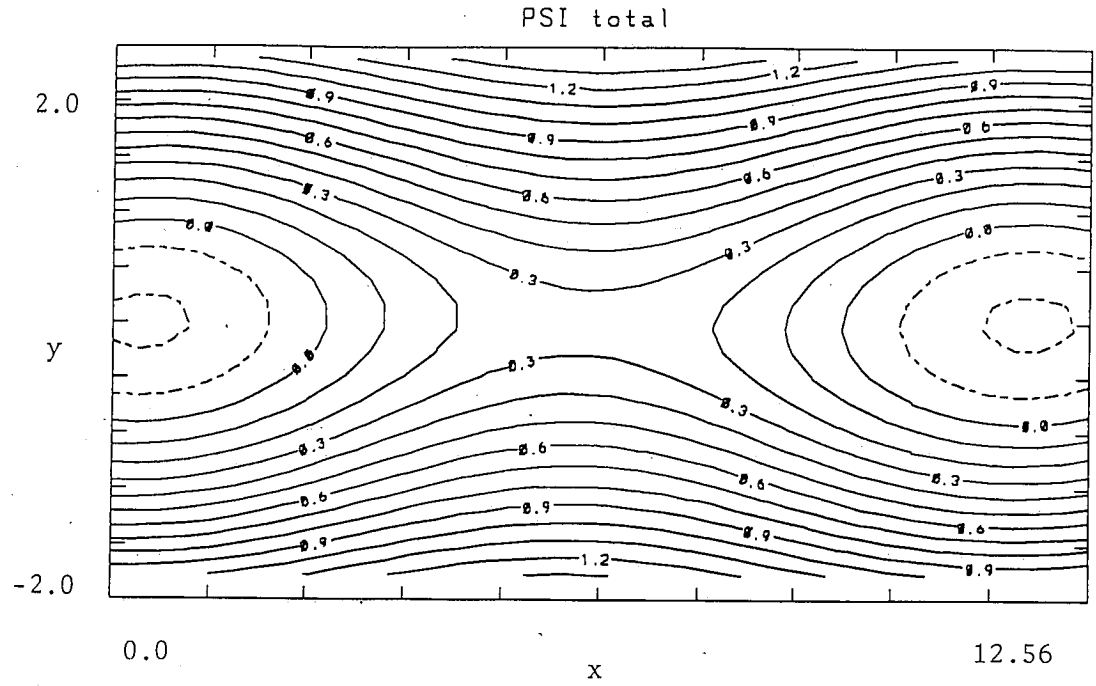

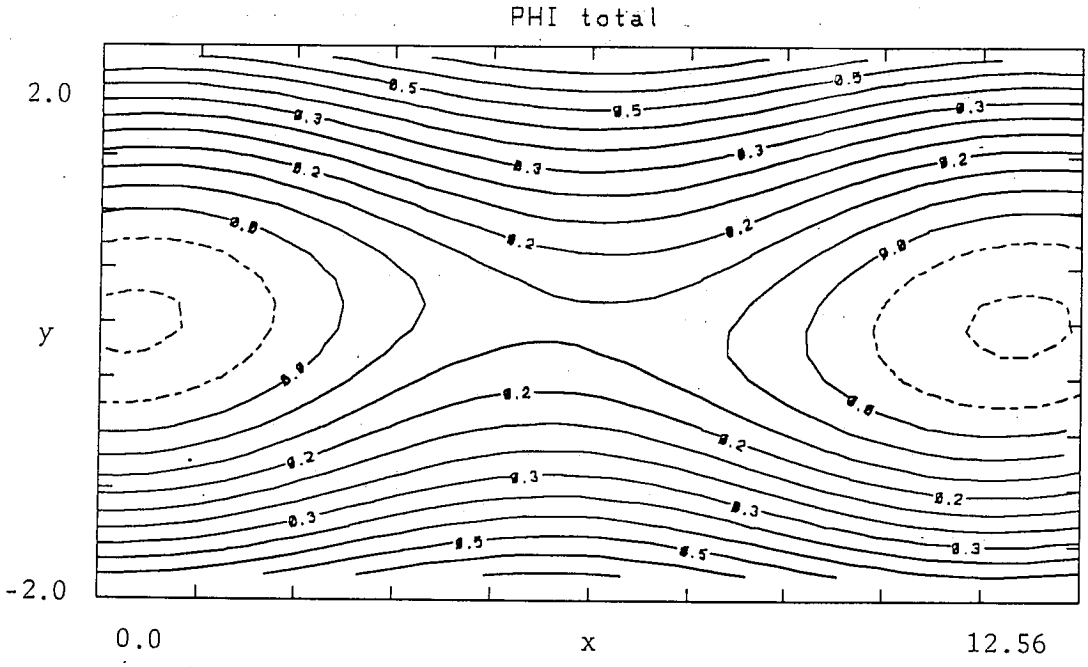

Fig. 4

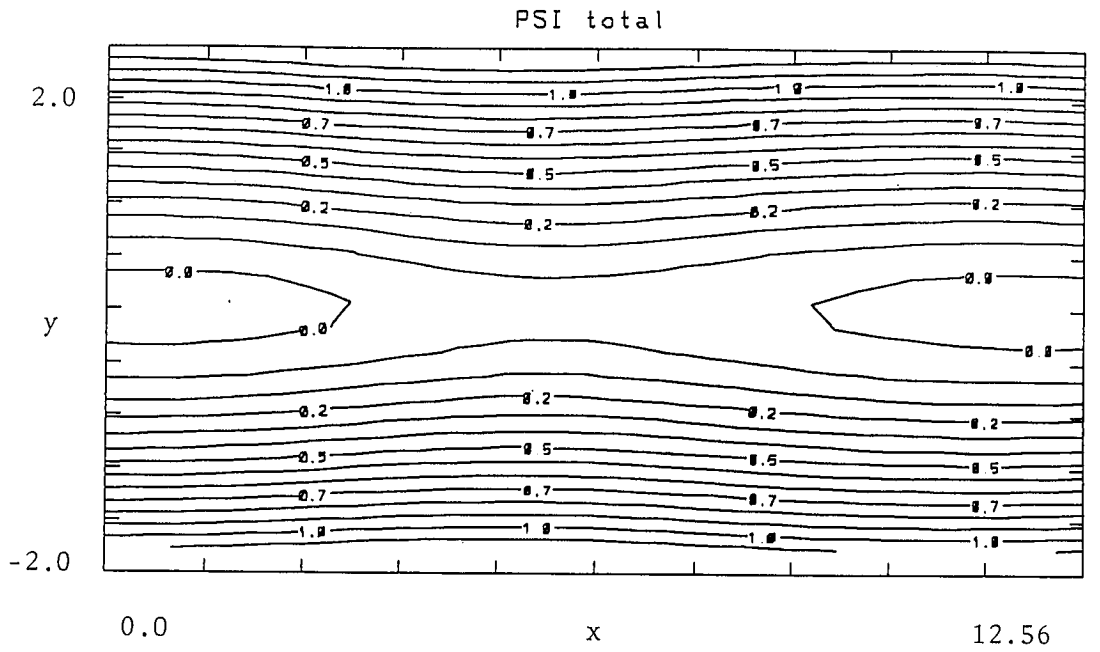

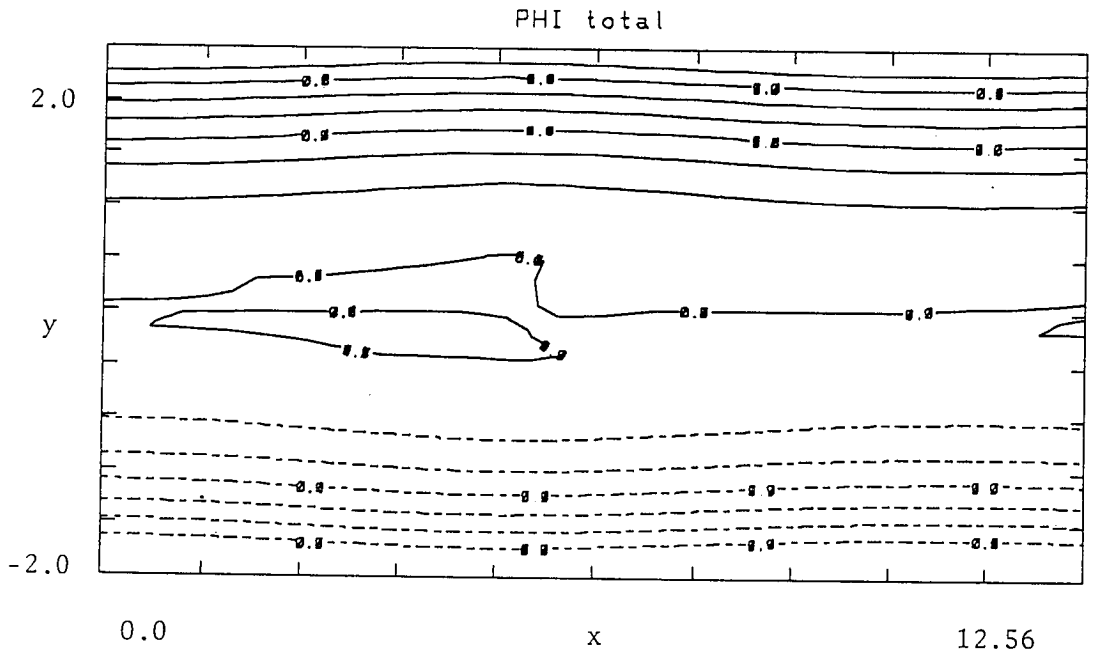

Fig. 5(a)

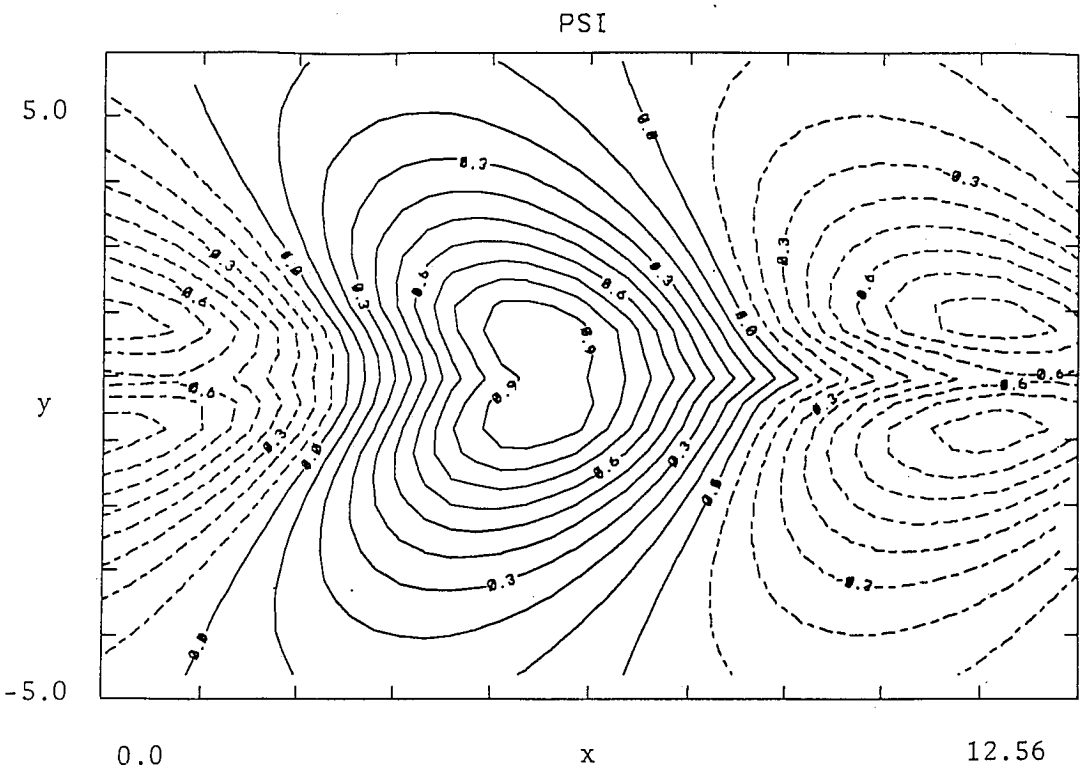

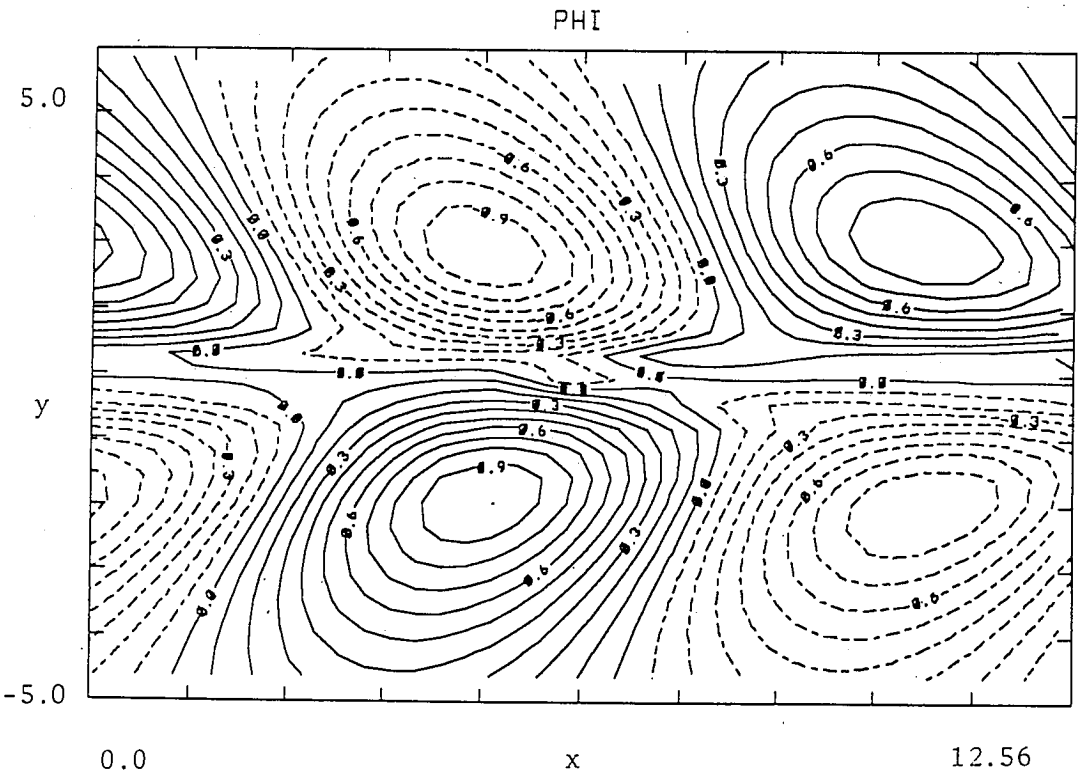

Fig. 5(b)

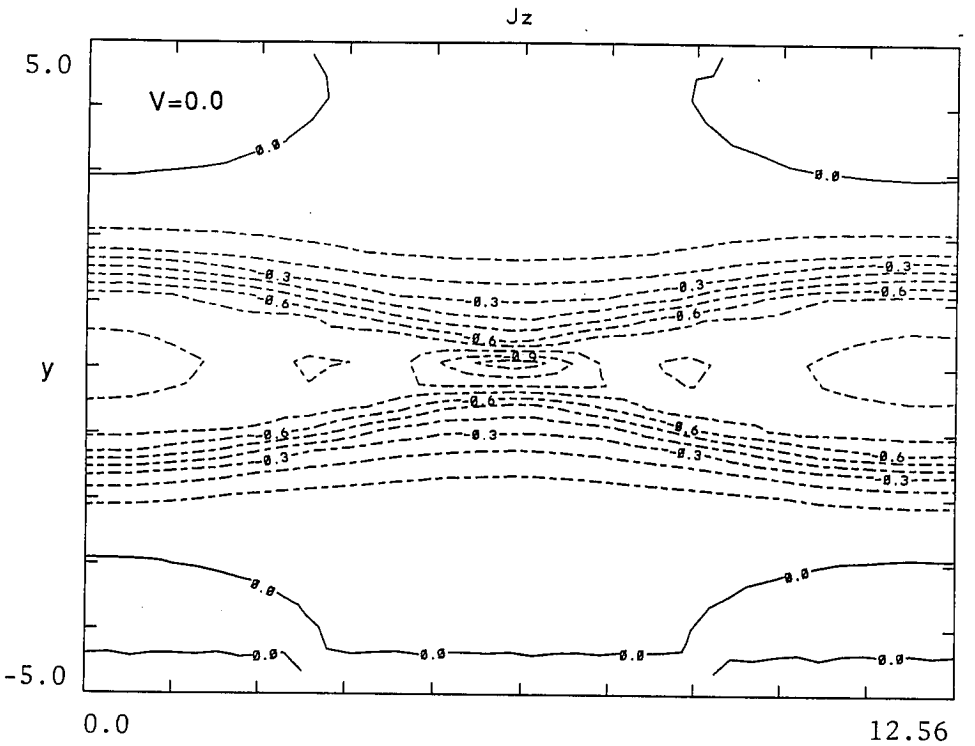

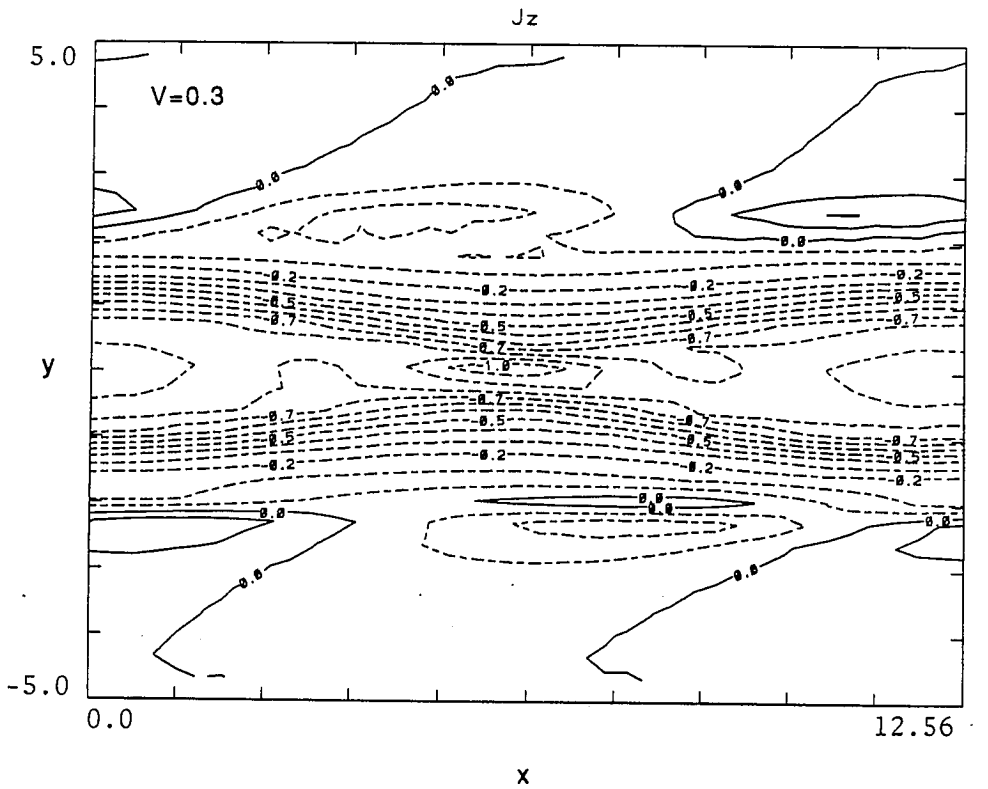

Fig. 6

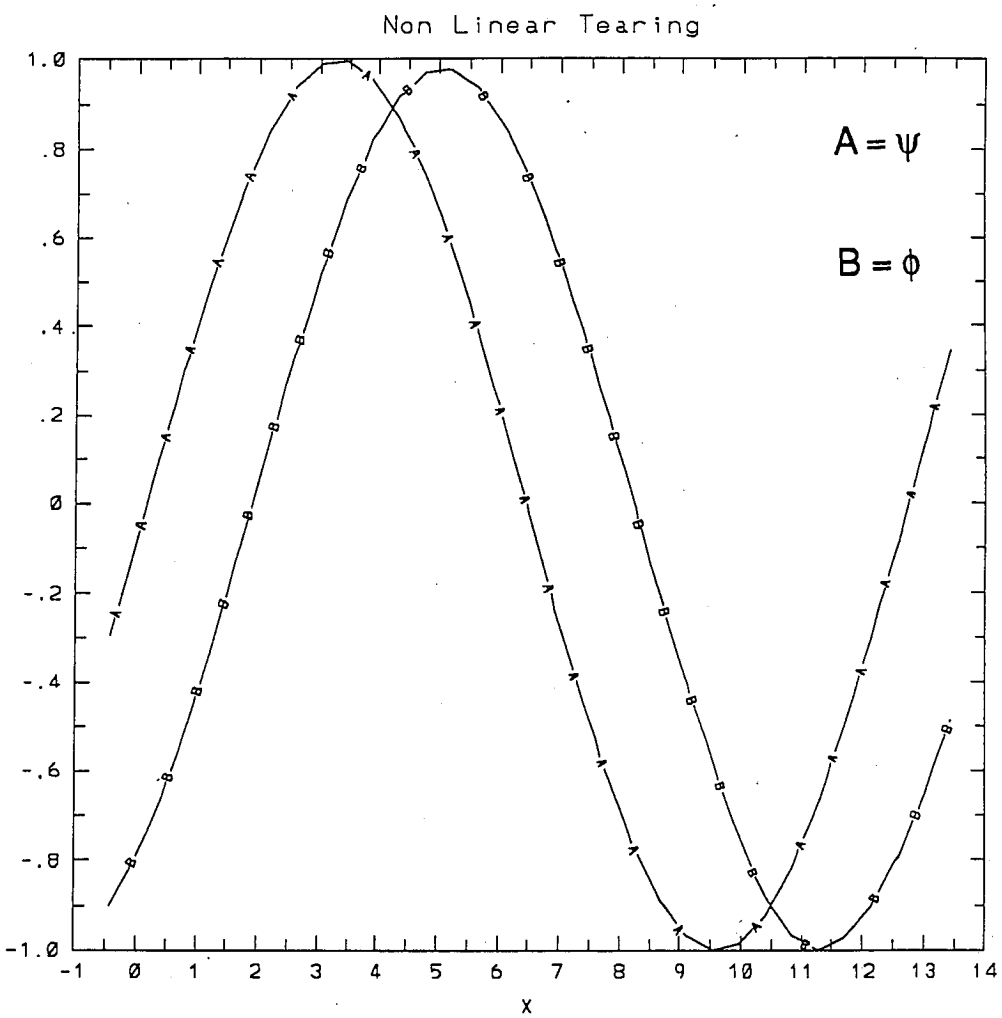
Non Linear Tearing
A = ψ
B = ϕ
1.0
.8
.6
.4
.2
0
-.2
-.4
-.6
-.8
-1.0
-1 0 1 2 3 4 5 6 7 8 9 10 11 12 13 14
X

Fig. 7

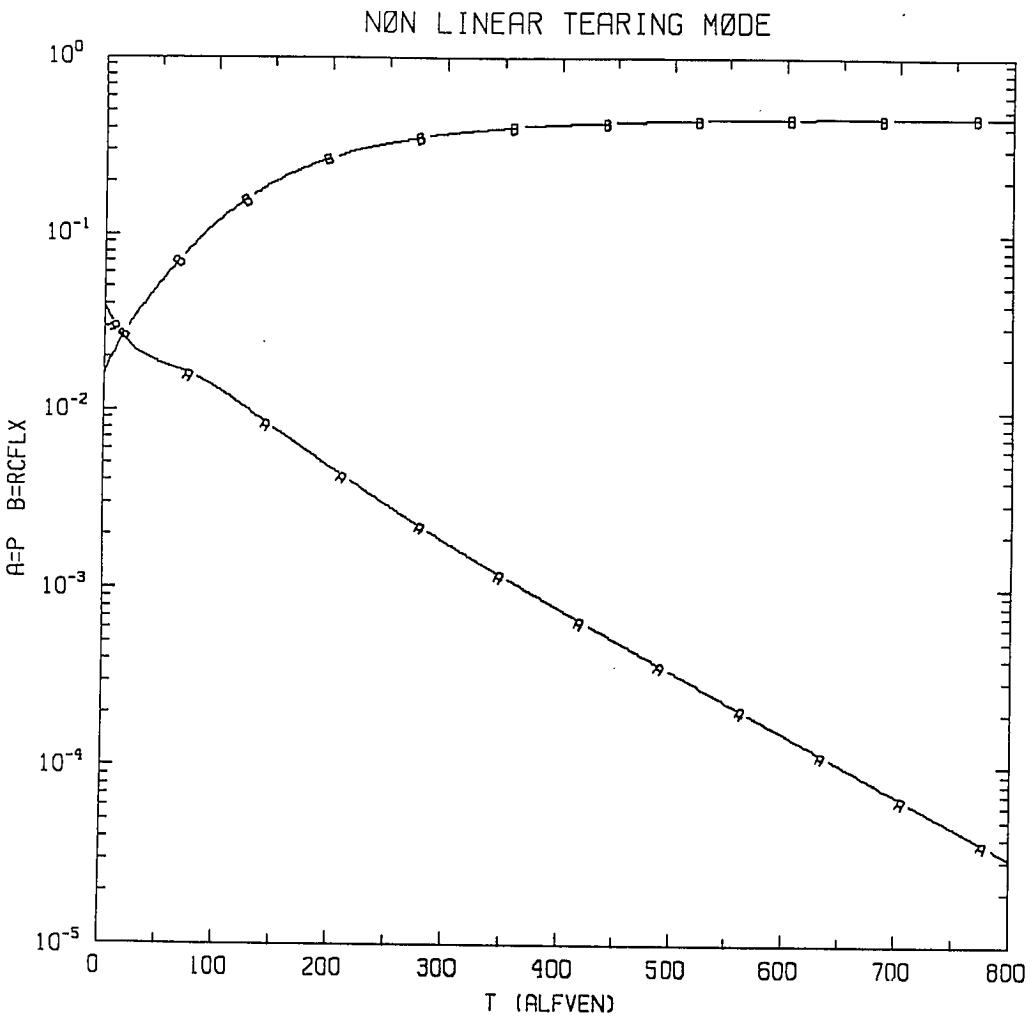
NØN LINEAR TEARING MØDE
A=P B=RCFLX
T (ALFVEN)
10^0
10^-1
10^-2
10^-3
10^-4
10^-5
0
100
200
300
400
500
600
700
800

Fig. 8(a)

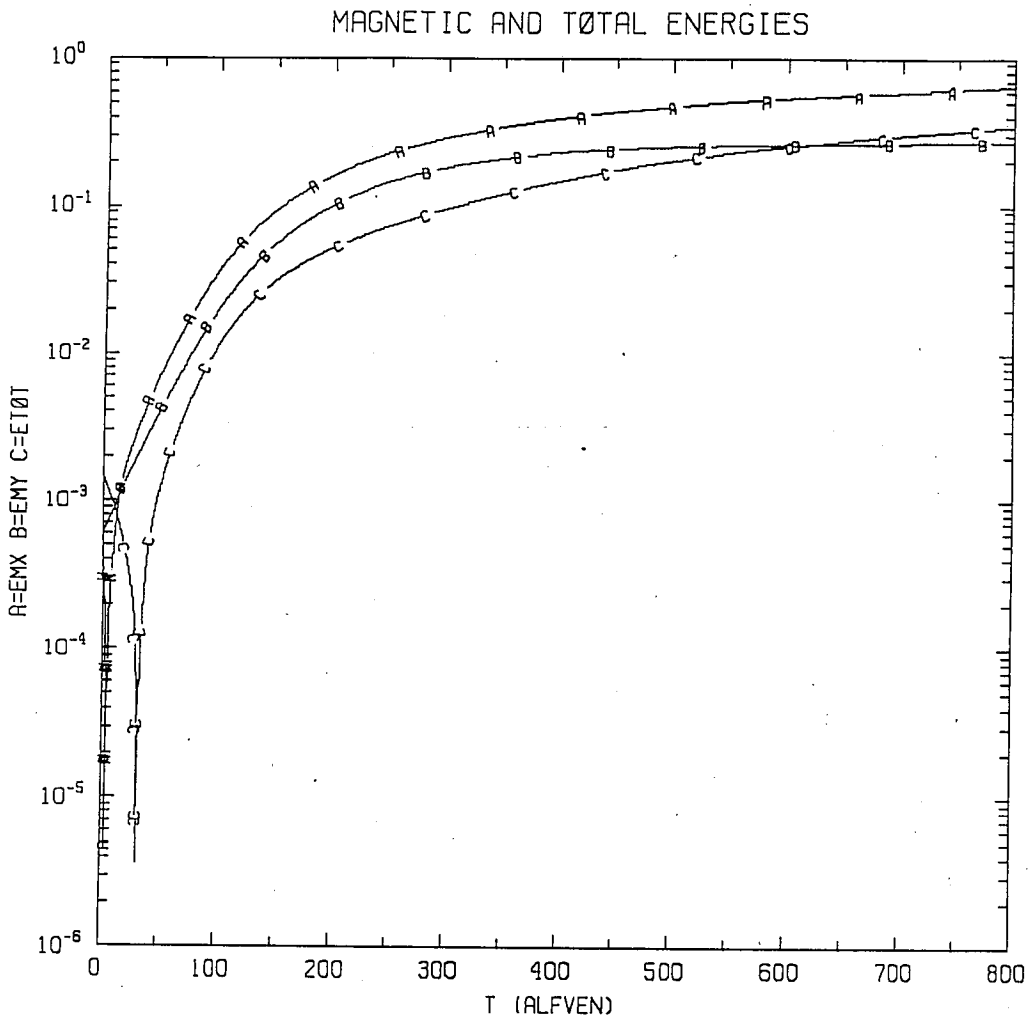
MAGNETIC AND TØTAL ENERGIES
A=EMX B=EMY C=ETØT
T (ALFVEN)
10^0
10^-1
10^-2
10^-3
10^-4
10^-5
10^-6
0
100
200
300
400
500
600
700
800

Fig. 8(b)

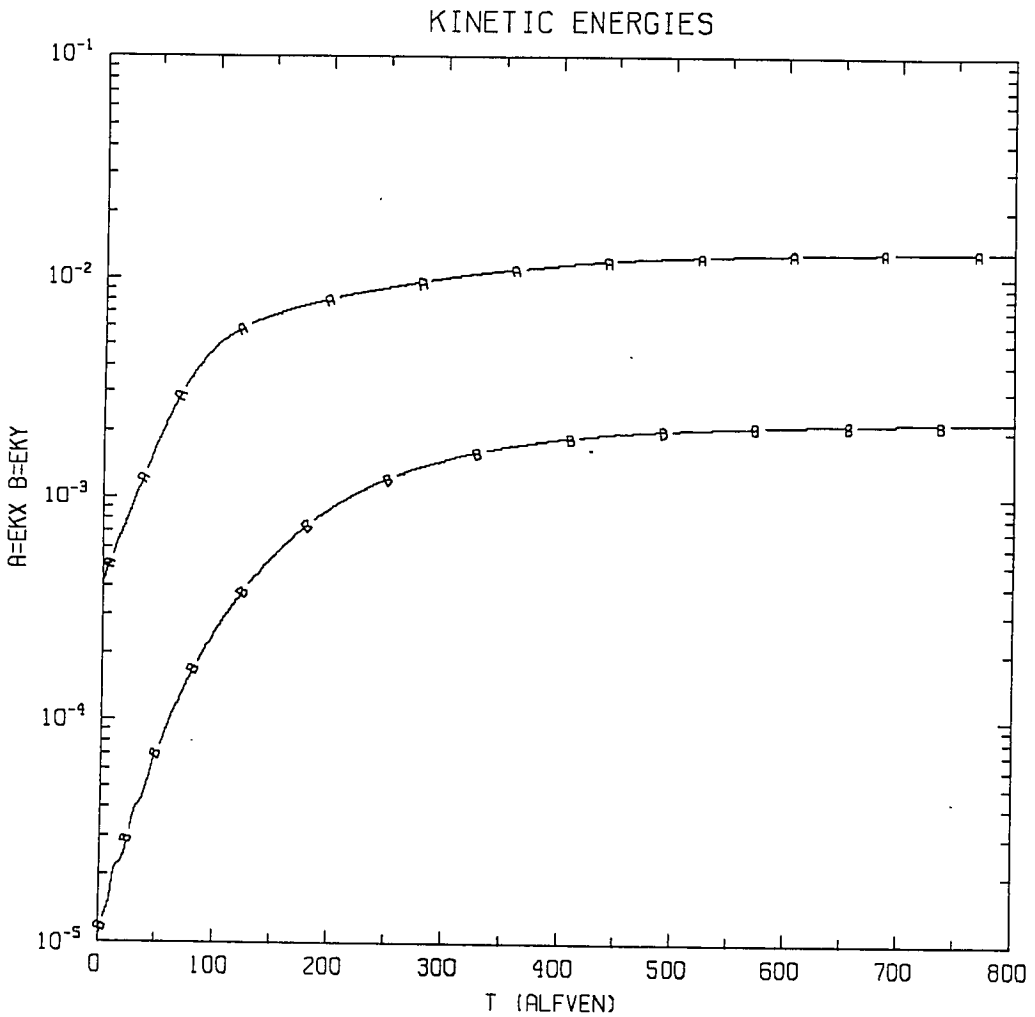
KINETIC ENERGIES
A=EKX B=EKY
10^{-1}
10^{-2}
10^{-3}
10^{-4}
10^{-5}
0
100
200
300
400
500
600
700
800
T (ALFVEN)

Fig. 8(c)

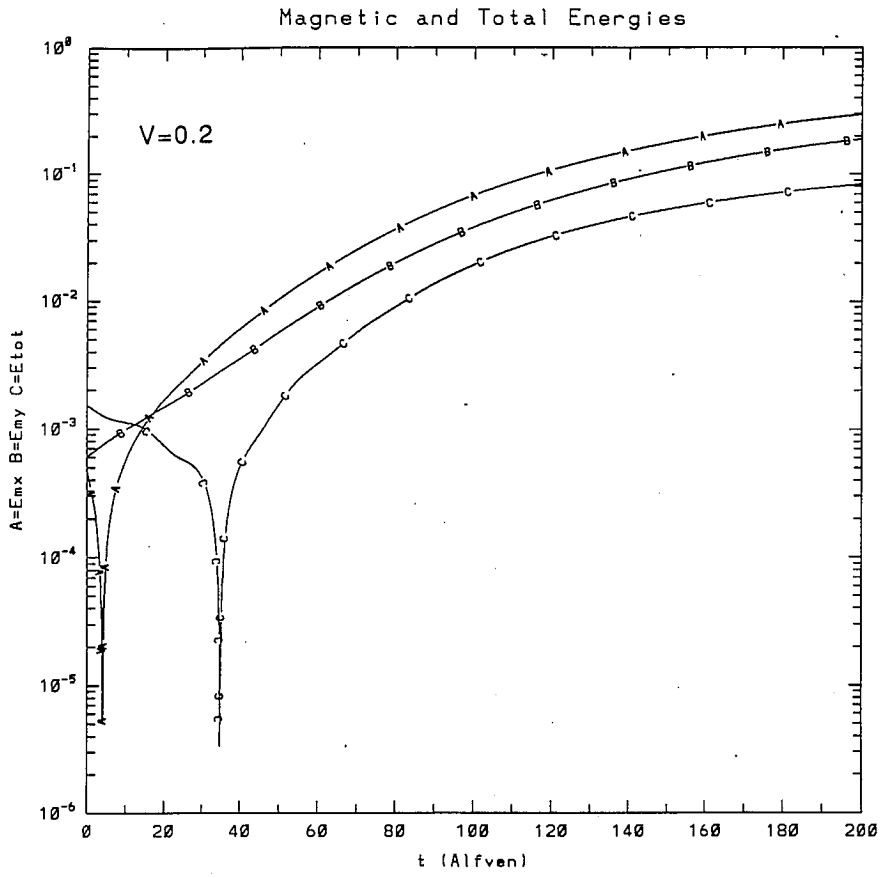
Magnetic and Total Energies
V=0.2
A=Emx B=Emy C=Etot
t (Alfven)

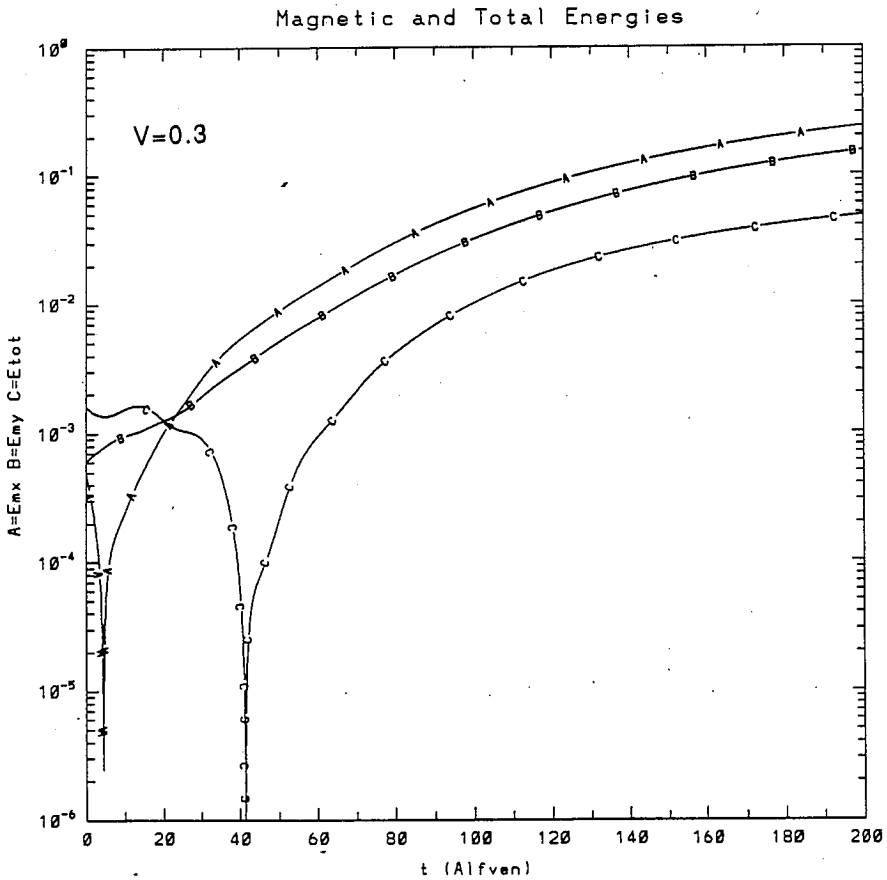
Magnetic and Total Energies
V=0.3
A=Emx B=Emy C=Etot
t (Alfven)

Fig. 9

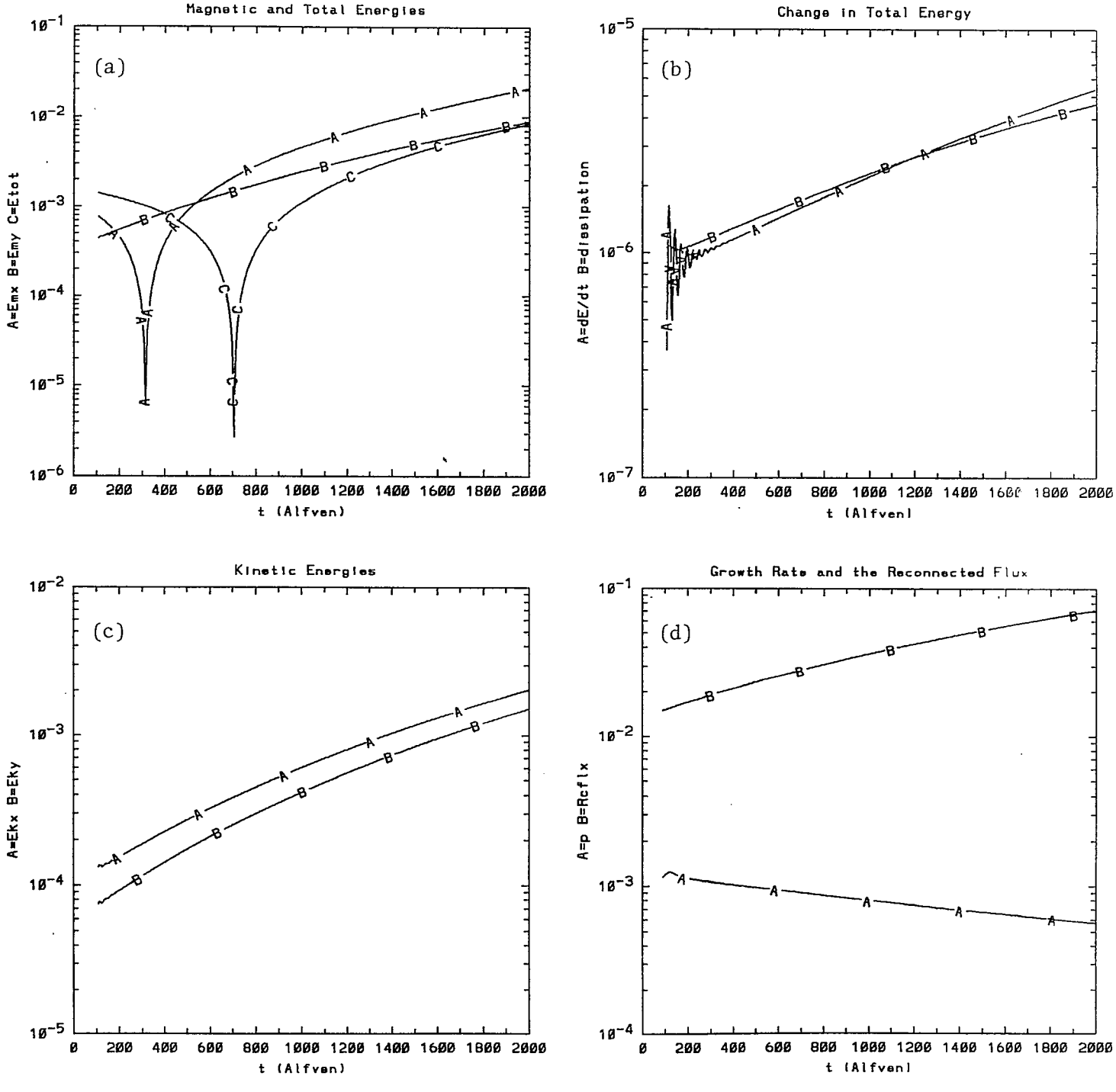
Magnetic and Total Energies
(a)
A=Emx B=Emy C=Etot
t (Alfven)
Change in Total Energy
(b)
A=dE/dt B=dissipation
t (Alfven)
Kinetic Energies
(c)
A=Ekx B=Eky
t (Alfven)
Growth Rate and the Reconnected Flux
(d)
A=p B=Rcflx
t (Alfven)

Fig. 10

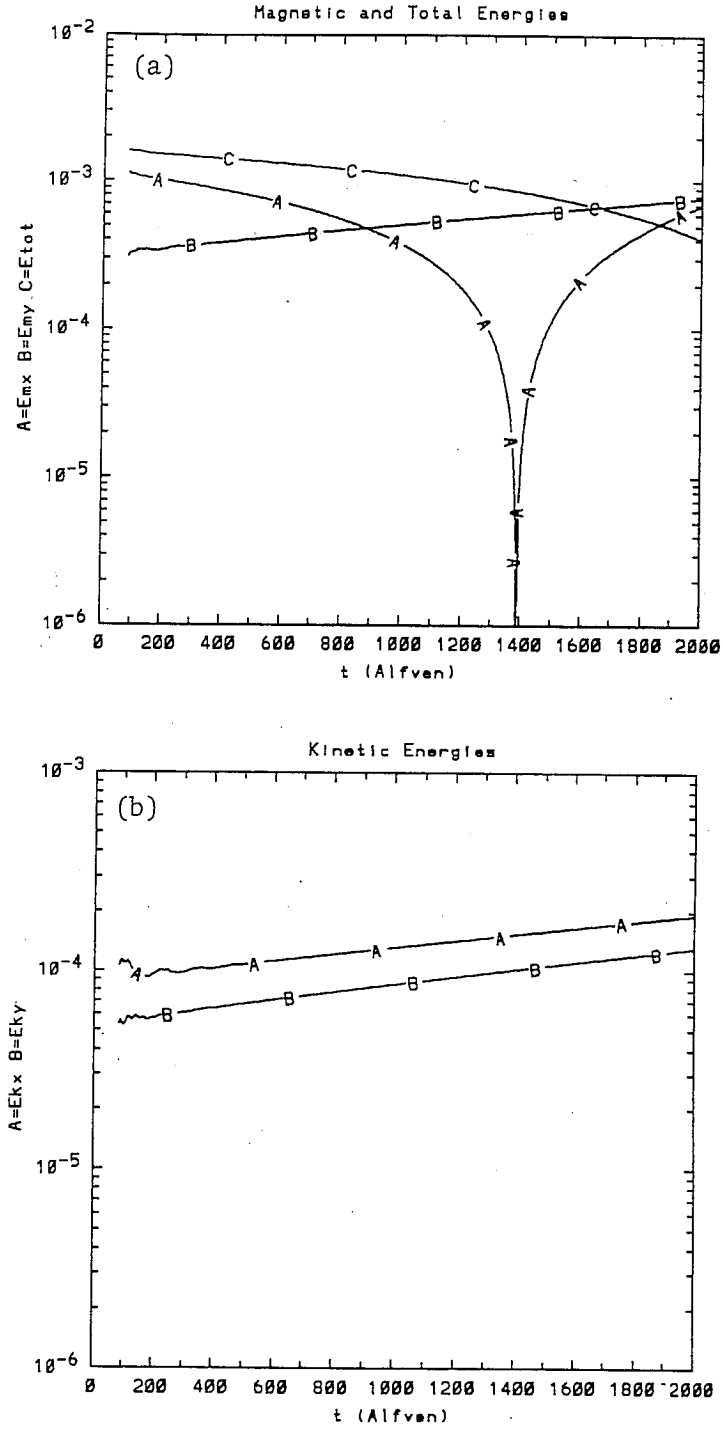
Magnetic and Total Energies
(a)
A=Emx B=Emy C=Etot
t (Alfven)
Kinetic Energies
(b)
A=Ekx B=Eky
t (Alfven)

Fig. 11

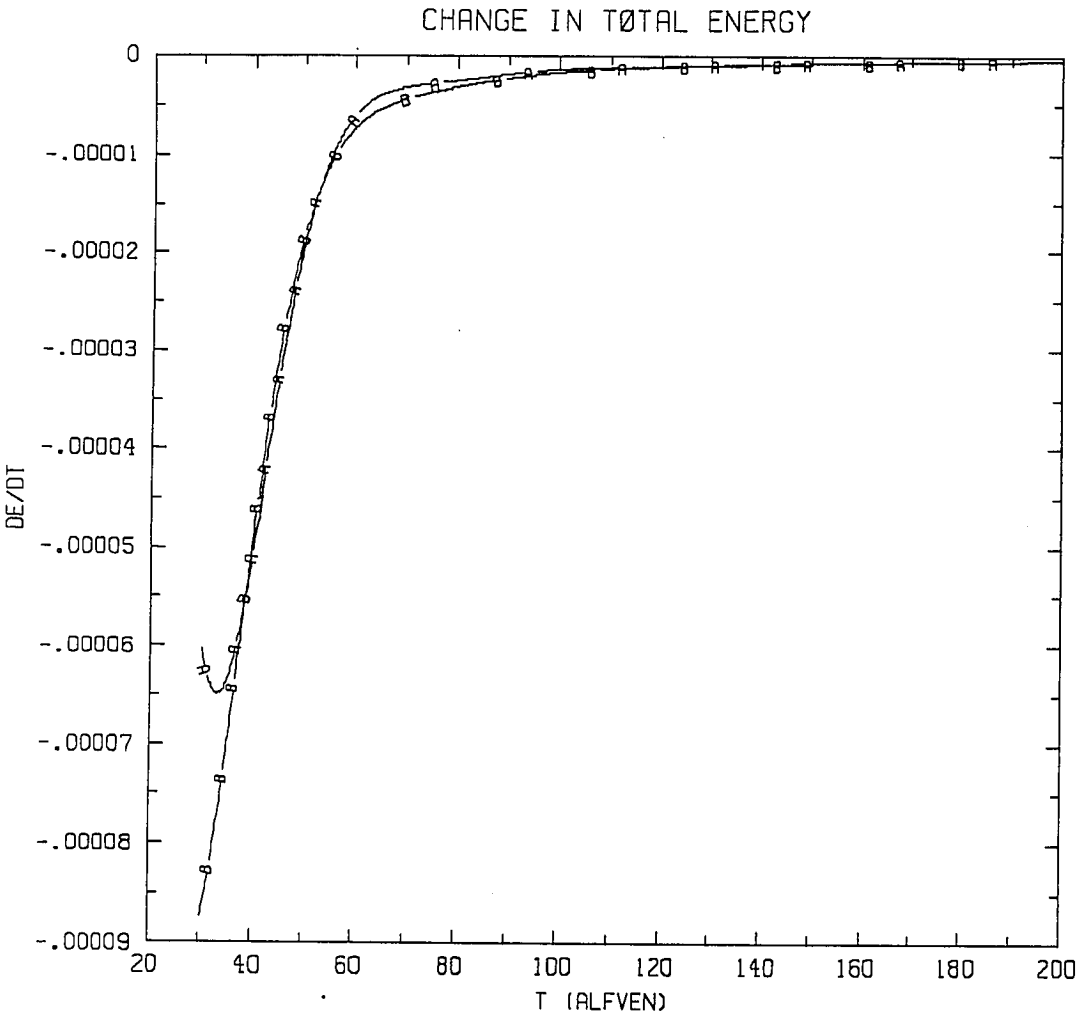
CHANGE IN TØTAL ENERGY
0
-.00001
-.00002
-.00003
-.00004
-.00005
-.00006
-.00007
-.00008
-.00009
DE/DT
20
40
60
80
100
120
140
160
180
200
T (ALFVEN)

Fig. 12(a)

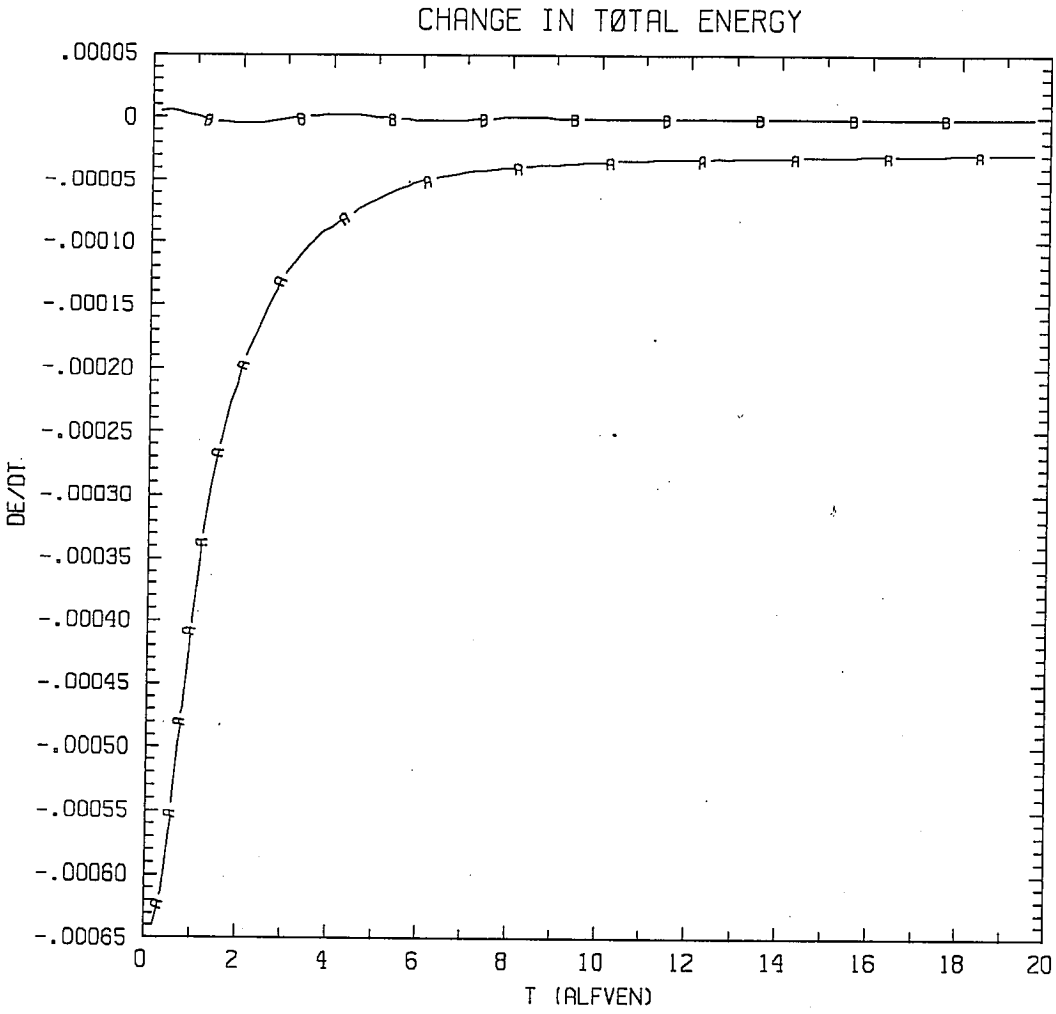
CHANGE IN TØTAL ENERGY
.00005
0
-.00005
-.00010
-.00015
-.00020
-.00025
-.00030
-.00035
-.00040
-.00045
-.00050
-.00055
-.00060
-.00065
DE/DT
0
2
4
6
8
10
12
14
16
18
20
T (ALFVEN)

Fig. 12(b)